J. Fluid Mech. (1989), *vol.* 205, *pp.* 1–43
Printed in Great Britain

Dynamics of vortex interaction with a density interface

By WERNER J. A. DAHM[1], CHRISTINE M. SCHEIL[1] AND GRÉTAR TRYGGVASON[2]

[1] Department of Aerospace Engineering, The University of Michigan, Ann Arbor, MI 48109-2140, USA

[2] Department of Mechanical Engineering and Applied Mechanics, The University of Michigan, Ann Arbor, MI 48109-2125, USA

(Received 6 July 1988)

We present results from an experimental and numerical investigation into the dynamics of the interaction between a planar vortex pair or axisymmetric vortex ring with lengthscale a and circulation Γ encountering a planar interface of thickness δ across which the fluid density increases from ρ_1 to ρ_2. Similarity considerations indicate that baroclinic generation of vorticity and its subsequent interaction with the original vortex is governed by two dimensionless parameters, namely $(a/\delta)A$ and R, where $A \equiv (\rho_2-\rho_1)/(\rho_2+\rho_1)$ and $R \equiv (a^3g/\Gamma^2)$. For thin interfaces ($\delta \ll a$), the interaction is governed only by the parameters A and R. Furthermore, in the Boussinesq limit ($A \to 0$), the dynamics are governed solely by the product AR and the interaction is entirely invertible with respect to the initial locations and direction of propagation of the vortices. We document details of the interaction dynamics in the Boussinesq limit over a range of the parameter AR. Results show that, for relatively small values of AR, rather than the vortex simply rebounding at the interface, its outermost layers are instead successively 'peeled' away by baroclinically generated vorticity and form a topologically complex backflow in which the ring fluid, the light fluid and the heavy fluid are intertwined. For larger values of AR the vortex barely penetrates the interface, and our results suggest that in the limit $AR \to \infty$ the interaction with a density interface becomes similar to the interaction at a solid wall. We also present results for thick interfaces in the Boussinesq limit, as well as larger density jumps for which the density parameter A enters as a second similarity quantity. Comparison of the experimental and numerical results demonstrate that many of the features of such interactions can be understood within the context of inviscid fluids, and that inviscid vortex methods can be used to accurately simulate the dynamics of such interactions.

1. Introduction

The dynamics of vorticity in uniform density fluids are fairly well established, and a variety of numerical techniques generally referred to under the collective term 'vortex methods' can be used to simulate many features of such flows. In particular, understanding of the dynamics of vorticity in two-dimensional flows of a uniform density fluid has matured to the point that accurate numerical simulation of many experimentally observed phenomena can be routinely done. A review of some of these phenomena is presented by Saffman & Baker (1979), and Leonard (1980) gives an overview of vortex methods for numerically simulating such two-dimensional

homogeneous flows. Progress is also being made in the development of vortex methods for axisymmetric and fully three-dimensional flows with uniform density. Some of these methods are reviewed by Leonard (1985).

However, many practical circumstances involve the dynamics of vorticity in fluids with non-uniform density. In flows of this type, vorticity can be generated in regions of non-zero density gradient when the centre of mass of a given fluid element does not coincide with the centre of force resulting from the pressure and viscous stresses acting over its surface. The subsequent interactions between the original vortical flow and the generated vorticity can give rise to entirely different dynamical phenomena. Such interactions are common both in nature and in technological applications. Examples include shock-wave interactions with vorticity, the interaction of a turbulent flow with a flame front, the motion of convective thermals encountering an atmospheric inversion layer, the interaction of a ship wake with a thermocline, etc. Much of the work to date on the dynamics of vorticity in flows with non-uniform density has centred on free-surface flows and on interfacial instabilities such as the Rayleigh–Taylor instability and the fingering instabilities in Hele-Shaw flow. In these cases, the vorticity is essentially confined to the interface and the remaining fluid is irrotational. However, the types of flows referred to above involve the direct interaction of a vortical flow with a density inhomogeneity. Previous investigations into this class of flows appear to have been largely motivated by interest in relatively weak atmospheric stratification on the propagation and development of aircraft trailing vortices. For example, Saffman (1972) describes the motion of a vortex pair in a weakly stratified fluid, for which Hill (1975) presents numerical calculations using vortex elements. Hecht *et al.* (1980, 1981) give computational results based on closure modelling of turbulent vortex pairs and rings propagating through various stratification conditions. Sarpkaya (1983) describes experiments which include the propagation of trailing vortex pairs through a stratified medium, and Maxworthy (1977) presents results from an experiment on the motion of a turbulent vortex ring propagating through a fluid with a very weak uniform density gradient.

In contrast, relatively little work has been reported for the interaction of vorticity with comparatively sharp density gradients. The case when the density jump is large, and in particular when the interface is a free surface with effectively zero density on one side, has received some attention (Saffman 1979). Krauch (1980) and Cerra & Smith (1983) have reported experimental results for a vortex ring rising toward a free surface, and Sarpkaya (1983) gives experimental results for the interaction of trailing vortex pairs with a free surface. Such free-surface interactions have also been addressed computationally (e.g. Tryggvason 1988*a*). Linden (1973) presents some experimental results for turbulent vortex rings encountering weak density interfaces, but does not elaborate on any details of the interaction dynamics.

Here we examine in detail the dynamics resulting from the interaction of vorticity with a relatively sharp density interface. The principal goals are to understand the mechanisms by which baroclinically generated vorticity interacts with vorticity already present in the flow and to document some of the dynamical features encountered in such interactions. In order to study the interaction in as controlled a setting as possible, we concentrate on two relatively simple vortical flows, namely the planar laminar vortex pair and the axisymmetric laminar vortex ring, and examine their interaction with a planar density interface. The dynamics of thin-cored vortex pairs and rings in the absence of any density interface are relatively well understood. For example, Lamb (1945) and Batchelor (1967) describe the

characteristics of inviscid vortex pairs and rings. Saffman (1970) and Fraenkel (1970) give the propagation velocity of the inviscid ring for arbitrary but small core structures and Saffman (1970) also examines the effects of growth of the vortical core by viscous diffusion. Magarvey & MacLatchy (1964*a*), Maxworthy (1972, 1977) and Sullivan, Widnall & Ezekiel (1973) present experimental results for the formation, structure and propagation of viscous vortex rings. Yih (1975) has given analytical solutions for internally stratified vortex pairs and rings moving in a homogeneous fluid. Observations of the instability of vortex rings are presented, for example, by Krutzsch (1936, 1939) and Maxworthy (1977). Some of the stability characteristics of vortex rings are described by Tomokita (1936), Widnall & Sullivan (1973), Widnall, Bliss & Tsai (1974) and Saffman (1978). The corresponding stability of planar vortex pairs has been analysed by Crow (1970), and the effect of a strain field on the stability of a vortex filament is given by Moore & Saffman (1975).

In this study, we are mainly concerned with interfaces across which there is a relatively small density change. We use laboratory experiments to identify the underlying dynamical phenomena associated with the interaction of a vortex ring with a density interface. These results are also used to evaluate the capabilities of numerical techniques based on inviscid vortex methods for simulating these phenomena. The numerical simulations allow important details of the interaction to be investigated that are not directly accessible in the laboratory experiments, and allow exploration of parameter ranges that are beyond the reach of the experiments. A brief account of some of the work presented here was given at the 40th Annual Meeting of the Division of Fluid Dynamics of the American Physical Society (Dahm & Scheil 1987; Tryggvason 1987).

The paper is organized as follows. In §2 we introduce the relevant similarity parameters and discuss several limiting cases of particular interest. In §3 we describe the experimental and numerical techniques used, and in §4 present results for the interaction of axisymmetric vortex rings and planar vortex pairs with a planar density interface. A discussion of some of these results as well as conclusions are given in §5.

2. Similarity considerations

Figure 1 shows a schematic of the general problem being considered. A planar vortex pair with spacing a, or an axisymmetric vortex ring with diameter a, and with circulation Γ and a characteristic core dimension σ encounters an interface of thickness δ across which the fluid density increases from ρ_1 to ρ_2. The flow is taken to be incompressible and governed by the Navier–Stokes equations

$$\tilde{\rho}\frac{\mathrm{D}\tilde{\boldsymbol{u}}}{\mathrm{D}\tilde{t}} = -\tilde{\boldsymbol{\nabla}}\tilde{p} - \tilde{\rho}g\hat{\boldsymbol{j}} + \mu\tilde{\nabla}^2\tilde{\boldsymbol{u}}, \tag{1}$$

where the tildes denote dimensional variables. The viscosity μ is taken to be uniform. The pressure can be eliminated by taking the curl of (1), yielding the vorticity transport equation

$$\frac{\mathrm{D}\tilde{\boldsymbol{\omega}}}{\mathrm{D}\tilde{t}} = (\tilde{\boldsymbol{\omega}}\cdot\tilde{\boldsymbol{\nabla}})\tilde{\boldsymbol{u}} - \frac{\tilde{\boldsymbol{\nabla}}\tilde{\rho}}{\tilde{\rho}}\times\frac{\mathrm{D}\tilde{\boldsymbol{u}}}{\mathrm{D}\tilde{t}} - g\frac{\tilde{\boldsymbol{\nabla}}\tilde{\rho}}{\tilde{\rho}}\times\hat{\boldsymbol{j}} + \nu\tilde{\nabla}^2\tilde{\boldsymbol{\omega}}, \tag{2}$$

where the second and third terms on the right-hand side give the generation of vorticity resulting from pressure gradients and viscous stress gradients in an inhomogeneous fluid. When viscous effects are unimportant, these terms give the

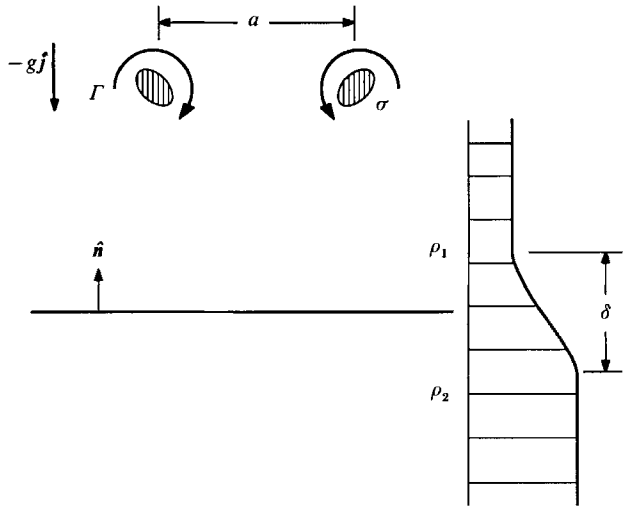

FIGURE 1. Notation for a planar vortex pair or an axisymmetric vortex ring, with circulation Γ and characteristic size a, approaching a planar interface with thickness δ across which the fluid density changes from ρ_1 to ρ_2. When the density change across the interface is small (the Boussinesq limit), the interaction is identical regardless of whether the vortex moves downward towards the heavy fluid or upward toward the light fluid, and is determined entirely by the parameter AR in (5).

vorticity produced by the hydrodystatic and hydrodynamic pressure gradients, commonly referred to as the baroclinic generation of vorticity.

To identify the relative importance of the various physical processes accounted for in (2), the dimensional variables are scaled with Γ and a as

$$\tilde{\boldsymbol{x}} = a\boldsymbol{x}, \quad \tilde{t} = (a^2/\Gamma)\cdot t, \quad \tilde{\boldsymbol{u}} = (\Gamma/a)\cdot\boldsymbol{u}, \quad \tilde{\boldsymbol{\omega}} = (\Gamma/a^2)\cdot\boldsymbol{\omega},$$

where the untilded variables are dimensionless and of order 1. The density is scaled with ρ_1 and ρ_2 as

$$\tilde{\rho} = (\rho_1+\rho_2)\cdot\rho,$$

and the density gradient in the baroclinic terms can be scaled as

$$\tilde{\boldsymbol{\nabla}}\tilde{\rho} = \frac{(\rho_1-\rho_2)}{\delta} f\left(\frac{y}{\delta/a}\right)\hat{\boldsymbol{n}},$$

where $\hat{\boldsymbol{n}}$ is a local unit normal vector relative to the interface. This scaling gives the vorticity transport equation as

$$\frac{\mathrm{D}\boldsymbol{\omega}}{\mathrm{D}t} = (\boldsymbol{\omega}\cdot\boldsymbol{\nabla})\boldsymbol{u} + \left[\frac{\rho_2-\rho_1}{\rho_2+\rho_1}\frac{a}{\delta}\right]\frac{1}{\rho} f\left(\frac{y}{\delta/a}\right)\hat{\boldsymbol{n}}\times\frac{\mathrm{D}\boldsymbol{u}}{\mathrm{D}t}$$
$$+\left[\frac{\rho_2-\rho_1}{\rho_2+\rho_1}\frac{a}{\delta}\frac{a^3 g}{\Gamma^2}\right]\frac{1}{\rho} f\left(\frac{y}{\delta/a}\right)\hat{\boldsymbol{n}}\times\hat{\boldsymbol{\jmath}} + \left[\frac{\nu}{\Gamma}\right]\nabla^2\boldsymbol{\omega}. \quad (3)$$

A similar scaling to characterize the surface tension T along the interface leads to the appropriate Weber number as

$$\left[\frac{(\rho_1+\rho_2)\,\Gamma^2}{aT}\right].$$

This reasoning suggests that similarity would require matching at least the four dimensionless parameters in square brackets, in addition to the initial density

gradient profile $f[y/(\delta/a)]$. Note that for vortex rings, the core parameter (σ/a) would also need to be matched, since in that case the diameter a and circulation Γ alone are not sufficient to characterize the motion (e.g. Lamb 1945; Batchelor 1967).

Among the range of values which these dimensionless parameters can assume, there are several limiting cases that are of particular physical significance and which are dominated by far less restrictive similarity requirements. For instance, when the Reynolds number (Γ/ν) in (3) is large, the distance over which vorticity can diffuse on the timescale (a^2/Γ) of the vortical motion is small relative to the lengthscale a. Effects of vorticity diffusion would then be of only secondary importance, and similarity might be effectively achieveable without precisely matching the Reynolds number. In such cases it may even be possible to understand many aspects of the interaction by treating the fluids as being inviscid. Similarly, the effects of surface tension on the resulting interaction dynamics can also be expected to be relatively unimportant if the Weber number is sufficiently large. In the remainder of this section, we examine the parameters controlling the dynamics under conditions for which the effects of viscosity and surface tension are negligible.

2.1. *Thin interfaces* $(\delta/a \to 0)$

When the interface thickness δ is small in comparison with the lengthscale a of the vortical motion, neither the precise interface thickness nor the details of the density or vorticity profiles within it should be important, and only the resulting circulation density along the interface should be dynamically relevant. Formally, as $(\delta/a) \to 0$ the density profile approaches a step function while the density gradient approaches a delta function $\delta(n)$ at the interface, where n is a local interface normal coordinate. Equation (3) can then be written as

$$\frac{\mathrm{D}\boldsymbol{\omega}}{\mathrm{D}t} = (\boldsymbol{\omega}\cdot\boldsymbol{\nabla})\,\boldsymbol{u} + 2\left[\frac{\rho_2-\rho_1}{\rho_2+\rho_1}\right]\hat{\boldsymbol{n}}\times\frac{\mathrm{D}\boldsymbol{u}}{\mathrm{D}t}\,\delta(n) + 2\left[\frac{\rho_2-\rho_1}{\rho_2+\rho_1}\,\frac{a^3 g}{\Gamma^2}\right]\hat{\boldsymbol{n}}\times\hat{\boldsymbol{j}}\,\delta(n), \tag{4}$$

which could be integrated across the interface to give the circulation density explicitly. The interaction with a thin interface is therefore governed by the two dimensionless parameters

$$A \equiv \left[\frac{\rho_2-\rho_1}{\rho_2+\rho_1}\right], \quad R \equiv \left[\frac{a^3 g}{\Gamma^2}\right]. \tag{5}$$

The first of these is simply the Atwood number, and gives the dimensionless density jump across the interface. The second gives the ratio of the hydrostatic to hydrodynamic pressure gradients for baroclinic generation of vorticity, and is effectively the inverse Froude number. In terms of A and R,

$$\frac{\mathrm{D}\boldsymbol{\omega}}{\mathrm{D}t} = (\boldsymbol{\omega}\cdot\boldsymbol{\nabla})\,\boldsymbol{u} + 2A\hat{\boldsymbol{n}}\times\frac{\mathrm{D}\boldsymbol{u}}{\mathrm{D}t}\,\delta(n) + 2AR\hat{\boldsymbol{n}}\times\hat{\boldsymbol{j}}\,\delta(n). \tag{6}$$

2.2. *Weak vortices* $(R \to \infty)$

Equation (6) describes the interaction of a vortex with arbitrary strength R encountering a thin interface with arbitrary strength A. Of particular interest is the case when R is large so that the product AR is also large, namely when the hydrostatic pressure gradients are much larger than the hydrodynamic gradients. Since both sides in (6) must be of order 1, the resulting interface slope $\hat{\boldsymbol{n}}\times\hat{\boldsymbol{j}}$ must then decrease like $1/AR$ to leading order. As a result, in the limit when $AR \to \infty$, the interface must remain flat $(\hat{\boldsymbol{n}}\times\hat{\boldsymbol{j}} \to 0)$ to leading order throughout the interaction.

This still admits the possibility that the product $AR\hat{\boldsymbol{n}}\times\hat{\boldsymbol{j}}\rightarrow$ constant, in which case baroclinic generation by the hydrostatic gradient will contribute to the interaction even though the interface is nominally flat. We examine this limit further in §4.6.

2.3. *Weak interfaces* ($A\rightarrow 0$)

For many practical situations the density stratification is relatively weak. In the limit as $A\rightarrow 0$, (6) reduces to

$$\frac{\mathrm{D}\boldsymbol{\omega}}{\mathrm{D}t}=\boldsymbol{\omega}\cdot\boldsymbol{\nabla}\boldsymbol{u}, \tag{7}$$

which simply demonstrates that the total circulation due to baroclinic generation of vorticity on the timescale (a^2/Γ) of the flow is small in comparison with Γ. As a result, on this timescale the vortex will propagate through the interface essentially undisturbed. Of course, on a much larger timescale, long after the vortex has penetrated through the interface, the baroclinic circulation will eventually become comparable to Γ.

This will remain the case except when $R\rightarrow\infty$, corresponding to a weak vortex encountering a weak interface, so that the product AR is no longer negligible. Equation (6) then reduces to

$$\frac{\mathrm{D}\boldsymbol{\omega}}{\mathrm{D}t}=\boldsymbol{\omega}\cdot\boldsymbol{\nabla}\boldsymbol{u}+2AR\hat{\boldsymbol{n}}\times\hat{\boldsymbol{j}}\delta(n), \tag{8}$$

which shows that essentially all the baroclinic generation in this limit is due to the hydrostatic pressure gradient only. The interaction is then determined by the single non-dimensional parameter AR. This is simply the Boussinesq limit, since the density variations are only important when combined with gravity. Notice also that the Boussinesq limit contains a certain symmetry not preserved by the full equation (3). If we consider a flow where the vortices are in the heavy fluid and propagate up toward the interface, this would be equivalent to replacing g by $-g$ and $\boldsymbol{\nabla}\rho$ by $-\boldsymbol{\nabla}\rho$ in the original flow. The net result is that the hydrostatic part of the baroclinic generation term in (3) remains unchanged. However, the hydrodynamic part changes sign, and so in general there is no similarity between these two flows. This will be true except in the Boussinesq limit given by (8), for which the hydrodynamic part is unimportant and as a result the evolution of both flows is identical. In the experiments and numerical simulations in §4, we examine the dynamics of the interaction in the Boussinesq limit over a range of values of AR for the case where the vortices are propagating downwards in the light fluid. Owing to the symmetry in this limit, the results are equally applicable to vortices propagating upward in the heavy fluid.

3. Experimental and numerical methods

In this section we describe the experimental and numerical methods used to study the interaction of vortex pairs and rings with a planar density interface. In practice, axisymmetric laminar vortex rings can be generated under very carefully controllable conditions in laboratory experiments, but practical difficulties associated principally with end effects render planar vortex pairs much more difficult to generate under similarly controllable conditions. Such vortex pairs can, however, be readily simulated using two-dimensional vortex methods. On the other hand, comparable simulations of vortex rings based on our current axisymmetric vortex method

require considerably more computational time. (Each of our two-dimensional simulations typically consume only about two minutes of CPU time on the SDSC Cray X-MP, while the axisymmetric simulations require more than half an hour.) By simulating two-dimensional vortex pairs we could investigate a larger number of cases for a relatively modest amount of computational time. For these reasons, the laboratory experiments have examined the interaction for vortex rings and the numerical simulations have focused largely on vortex pairs, though we also present a few results from axisymmetric simulations of vortex rings in §5. There are of course some differences in the dynamics of vortex pairs and rings, arising in large part from the importance of the detailed core structure even for thin-cored rings. However, since the core structure of the laboratory rings could not be precisely determined, conditions for the axisymmetric simulations could not be made identical to those in the experiments. We present the combined results from our laboratory experiments and numerical simulations in §4, where their similarities and differences are discussed.

3.1. *Experimental technique*

The experiments detail the interaction of vortex rings with a planar density interface. In all cases, the ring is formed from the light fluid and propagates downward through the light fluid towards the heavy fluid. Since these experiments are conducted entirely in the Boussinesq limit of small density parameter A, the results are also directly applicable to rings propagating upward toward a lighter fluid. In this limit the parameter AR characterizes the interaction, as discussed in §2.3. However, in dealing with vortex rings the core size (σ/a) also remains important, and as a result the association of a particular set of observed interaction dynamics with a particular value of AR must, strictly speaking, be limited to the specific core size used here. Nevertheless, the qualitative features of the resulting interaction dynamics should apply to a much larger class of such interactions. This is supported by results from the numerical simulations in §4.5.

Axisymmetric laminar vortex rings are formed in these experiments by symmetrically discharging a volume of fluid through a round nozzle to form a thin cylindrical sheet of vorticity. The vortex sheet rolls up and develops into a stable ring that propagates away from the nozzle. The ring fluid is discharged through a 4:1 area ratio contoured axisymmetric nozzle by driving its free surface in a plenum with a high-pressure air stream metered through a micrometer-controlled, variable throat orifice held at sonic conditions with a constant upstream pressure (80 p.s.i.g.). The plenum was designed with a large cross-sectional area (46.6 cm^2) and a small volume (149.5 cm^3) to allow the ring fluid to be accelerated rapidly. A solenoid valve is opened and closed via a variable-delay timing circuit to initiate the flow. For a given upstream pressure, the area of the sonic metering orifice sets the air flowrate into the plenum, and the solenoid delay time (typically 50–100 ms) sets the total amount of air supplied to the plenum. This pneumatically-driven arrangement allows for a very low disturbance level and a high degree of symmetry in the vortex sheet generation and roll-up processes which form the ring. Furthermore, the sonic metering valve and timing delay circuit allow for very fine control and precise repeatability in the ring formation.

Such a pressure-driven discharge system can, however, introduce oscillatory disturbances in the ring formation process if the spectral content of the pressure rise driving the ring fluid excites the natural frequency of the second-order system resulting from the compressibility of the air and the fluid mass in the plenum. In this facility, such oscillations have been effectively eliminated by scaling the system to

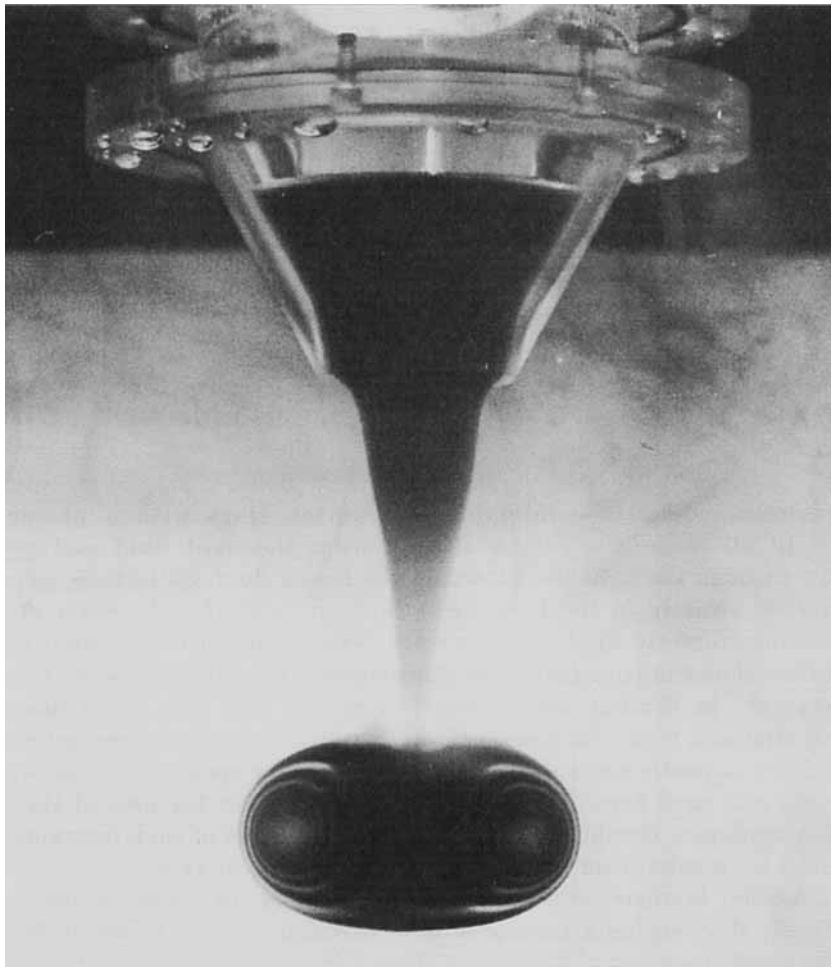

FIGURE 2. Typical axisymmetric laminar vortex ring generated in our experimental facility. The drive system ensures a very low disturbance level and a high degree of symmetry during the ring formation process, and allows for fine control and precise repeatability of the ring characteristics.

have a relatively high natural frequency and suppressing high frequencies in the pressure rise with a fluid equivalent of a low-pass filter (an adjustable volume of air in parallel with the plenum) tuned until no oscillations are evident.

The nozzle has an exit diameter of 3.9 cm and produces a ring with a centre-to-centre diameter $a \approx 4.9$ cm under all operating conditions. A typical ring is shown in figure 2. The nozzle exit velocity can be inferred from the displacement with time of the free surface in the plenum, which is recorded with large magnification on cine film using a macro lens. The ring circulation Γ is then estimated as the integral of the exit velocity with time. Saffman (1978) discusses some of the potential errors involved in such indirect estimates of the absolute circulation. In these experiments, however, the precise circulation for any given case is of lesser importance than its relation to other cases, and the present estimates are certainly adequate for this purpose. The resulting ring circulations range from 20 cm^2/s to 160 cm^2/s. A difficulty in generating rings with larger circulation is that a secondary ring begins to form that slowly travels downward and can interfere in the interaction of the original ring

with the interface. The core size σ is much more difficult to estimate, though for the technique used to generate the rings it appears reasonable to presume that σ will be of roughly the same order over this range of conditions. The corresponding Reynolds numbers (Γ/ν) in (3) range from 2000 to 16000, and the parameter R in (5) ranges from 4.3 to 275.

The reservoir into which the ring is introduced measures 30 cm on each side. The bottom half is filled with water mixed with salt or glycerine to render it heavier than the layer of fresh water on top. The density ratio A in (5) ranges from 0.001 to 0.03. These values should be sufficiently small to satisfy the Boussinesq limit in §2.3 and the interaction should therefore be determined by the parameter AR. Values of AR in these experiments cover the range from 0.014 to 1.20. To establish the interface, a water-soaked sheet of foam sponge material is placed on top of the heavy fluid and the light fluid then poured slowly onto it, allowing the light fluid to soak through with very little remaining momentum. As the tank fills, the foam floats on top of the light fluid and is finally removed, leaving behind two distinct fluid layers. This procedure allows us to routinely set up interfaces with thickness less than 2 mm ($\delta/a < 0.04$). By allowing the interface to diffuse for varying lengths of time, interfaces with differing thicknesses but having the same density gradient profile $f[y/(\delta/a)]$ can be investigated. For example, after approximately 26 h the interface achieves a thickness of about 5 cm ($\delta/a \approx 1$). Since the aqueous salt or glycerine mixtures are miscible with water, surface tension effects are negligible. Also, since the timescale on which gravity waves generated by the interaction propagate along the interface and reflect at the walls far exceeds the duration of the interaction, such waves do not interfere with the interaction.

The fluid moving with the vortex ring is made visible by dyeing the plenum fluid. In some cases we use food colour dye to allow observation of the entire ring and the three-dimensional structure resulting from the interaction. In other cases we observe the internal structure of the interaction in a cross-sectional plane using laser induced fluorescence (LIF) with a weak aqueous solution of disodium fluorescein dye for the ring fluid in conjunction with laser sheet illumination from a 5 W argon ion laser. In such cases, the heavy fluid contains a weak aqueous solution of Rhodamine B to allow simultaneous observation of the interface displacement. The ring motion and its interaction with the fluid interface are recorded with a motor driven 35 mm still camera at approximately 3 frames/s and with a 16 mm pin-register high-speed cine camera.

3.2. *Numerical methods*

The two-dimensional numerical simulations of vortex pairs reported here use an efficient Vortex-in-Cell (VIC) method for stratified flows discussed in detail by Tryggvason (1988*b*). We also present a few numerical simulations of vortex rings which use an axisymmetric direct summation vortex-blob method. Small-scale stabilization, generally essential for successful simulations with an inviscid model, is provided by the grid in the case of the VIC method, and by the blob size in the axisymmetric method. As far as regularization properties are concerned, the VIC method is nearly identical to blob methods, as discussed by Tryggvason (1989). The two-dimensional calculations assume a periodic box in the horizontal direction and no through-flow boundary conditions for the top and bottom boundaries. In most of our calculations the box is rather narrow, but some are repeated in a wider box and the differences discussed in §4.3. Most of the calculations are performed on a 32×64 mesh. Some are repeated on a finer mesh and the differences discussed in §4.4. For most of the calculations reported here, we use a circular vortex sheet located 5/3

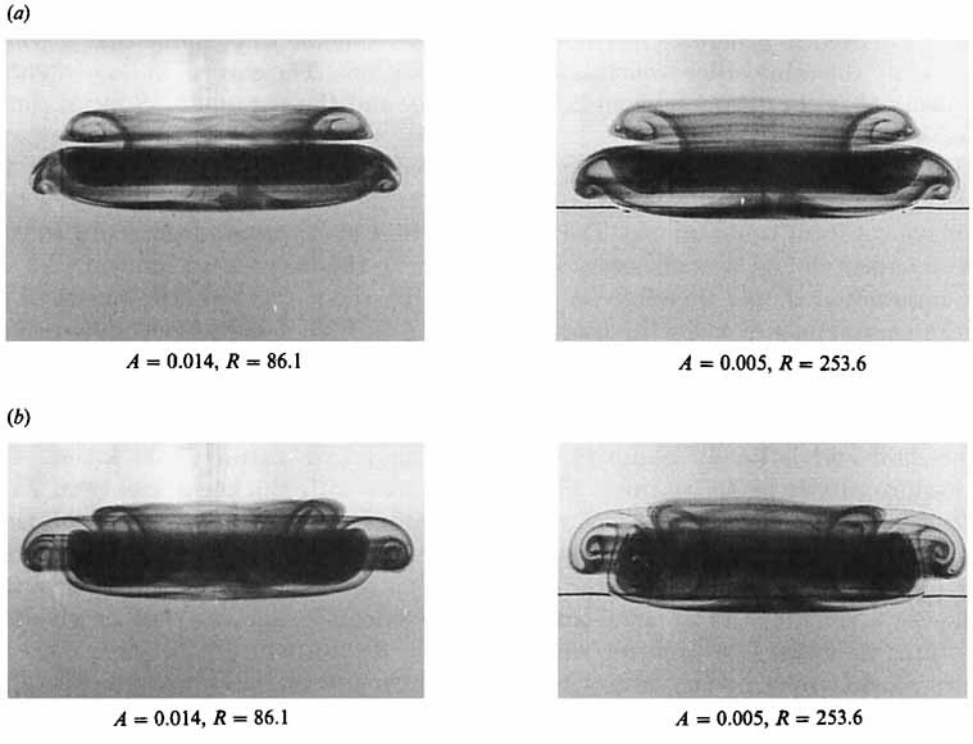

FIGURE 3. Test of similarity under the parameter AR, showing the interaction of a vortex ring for two different cases having $AR = 1.20$. The dimensionless times have been matched as closely as possible. Note that the interaction dynamics are essentially identical for both these cases. (a) Early time. (b) Later time.

radii above the density interface as the initial conditions (see first frame in figure 21). The vortex sheet strength is proportional to the sine of the angle measured from the forward stagnation point. This initially circular vortex sheet rolls up into two counter-rotating vortices, whose separation a is well estimated by assuming them to be point vortices and using the invariance of the first moment of vorticity. This gives $a \approx (\frac{1}{4}\pi)D$, where D is the initial diameter of the circular vortex sheet. Note that symmetry is not explicitly enforced in our calculations, although in most of our simulations symmetry is well preserved.

4. Results and discussion

4.1. *Test of similarity*

Before presenting detailed results documenting the interaction dynamics for thin interfaces in the Boussinesq limit over a range of values for the parameter AR, we first test the similarity of the flow under this parameter as discussed in §2.3. Figure 3 shows the interaction for two different cases characterized by the same value of AR at two different times. In both cases, the interface thickness $(\delta/a) < 0.04$ is considered sufficiently thin to be viewed in the thin interface limit of §2.1, and the density parameter $A < 0.014$ is considered sufficiently small to be viewed in the Boussinesq limit of §2.3. The dynamics in both cases should therefore be governed solely by the parameter AR. Figure 3(a) shows the early time development, while figure 3(b) shows the development at a later time. In the photographs on the left

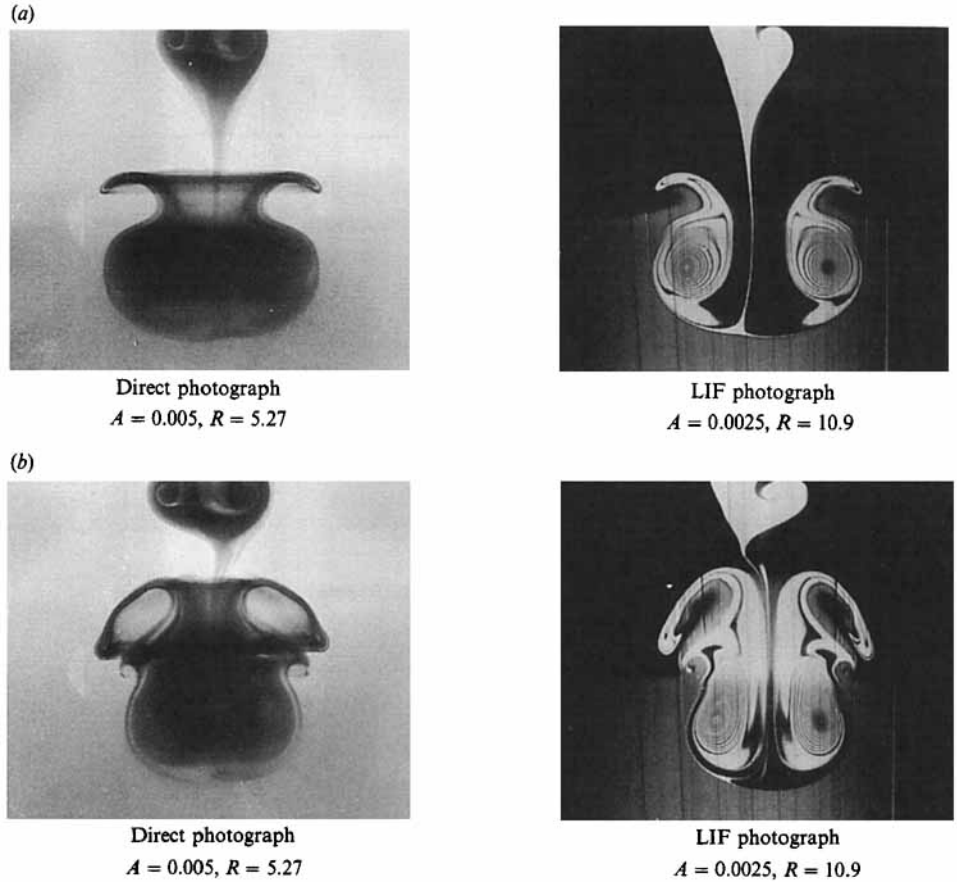

FIGURE 4. Further test of similarity under the parameter AR, showing the interaction of a vortex ring for two different cases having $AR = 0.025$. Note that the interaction dynamics are again essentially identical in these two cases, and are quite different from those seen for $AR = 1.20$ in figure 3. (*a*) Early time. (*b*) Later time.

$A = 0.014$ and $R = 86.1$, while on the right $A = 0.005$ and $R = 253.6$. In both cases $AR = 1.20$. The straight line in each photograph shows the initial position of the interface. The dimensionless times $(\Gamma/a^2)\tilde{t}$ have been matched as closely as possible in each comparison. We postpone a detailed discussion of the interaction dynamics until the following section. For the purposes of this section, it is sufficient to note that the comparisons in figure 3 show essentially the same features for both these interactions. (The appearance of wave-like features on the secondary ring in the photographs on the left are attributed to the Reynolds number dependence of an instability discussed in §4.2. Note that the Reynolds numbers are not matched in these two cases.) A further test of similarity for $AR = 0.025$ is shown in figures 4(*a*) and 4(*b*), with direct photographs showing the case $A = 0.005$ and $R = 5.27$ on the left, and with cross-sectional LIF photographs showing the corresponding internal structure for the case $A = 0.0025$ and $R = 10.9$ on the right. The comparisons in figures 4(*a*) and 4(*b*) again show that the detailed features of the interaction are virtually identical in both cases. Furthermore, a comparison between figures 3 and 4 also shows that the interaction dynamics are quite different in these two cases owing to their different values of AR. These results confirm the similarity arguments

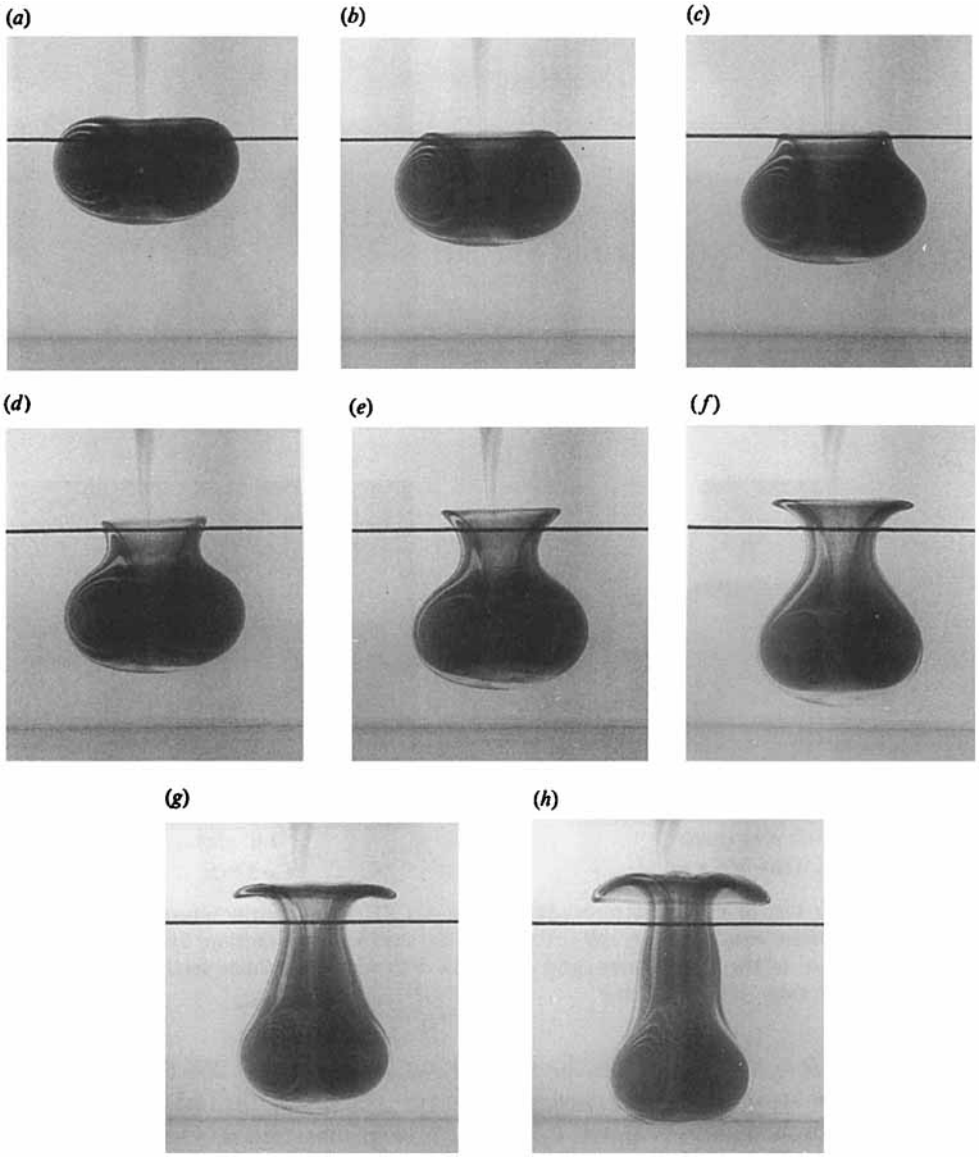

FIGURE 5. Photographic sequence showing vortex ring interaction for $AR = 0.014$ (Case 1 in table 1). The dark line shows the initial position of the interface. Such relatively small values of AR are characterized by the ring penetrating completely through the interface and well into the bottom fluid. Notice that the ring fluid is continuously stripped away at the sides of the crater and ejected back toward the top fluid. For smaller values of AR, the interaction is similar but the vortex penetrates further before the ring fluid is completely stripped away.

in §2.3 that the interaction for thin interfaces in the Boussinesq limit is determined by the single non-dimensional parameter AR.

4.2. *Interaction dynamics in the thin-interface limit*

In this section, we present results from experiments and numerical simulations documenting the interaction dynamics for thin interfaces in the Boussinesq limit over a wide range of the parameter AR. Four representative photographic sequences

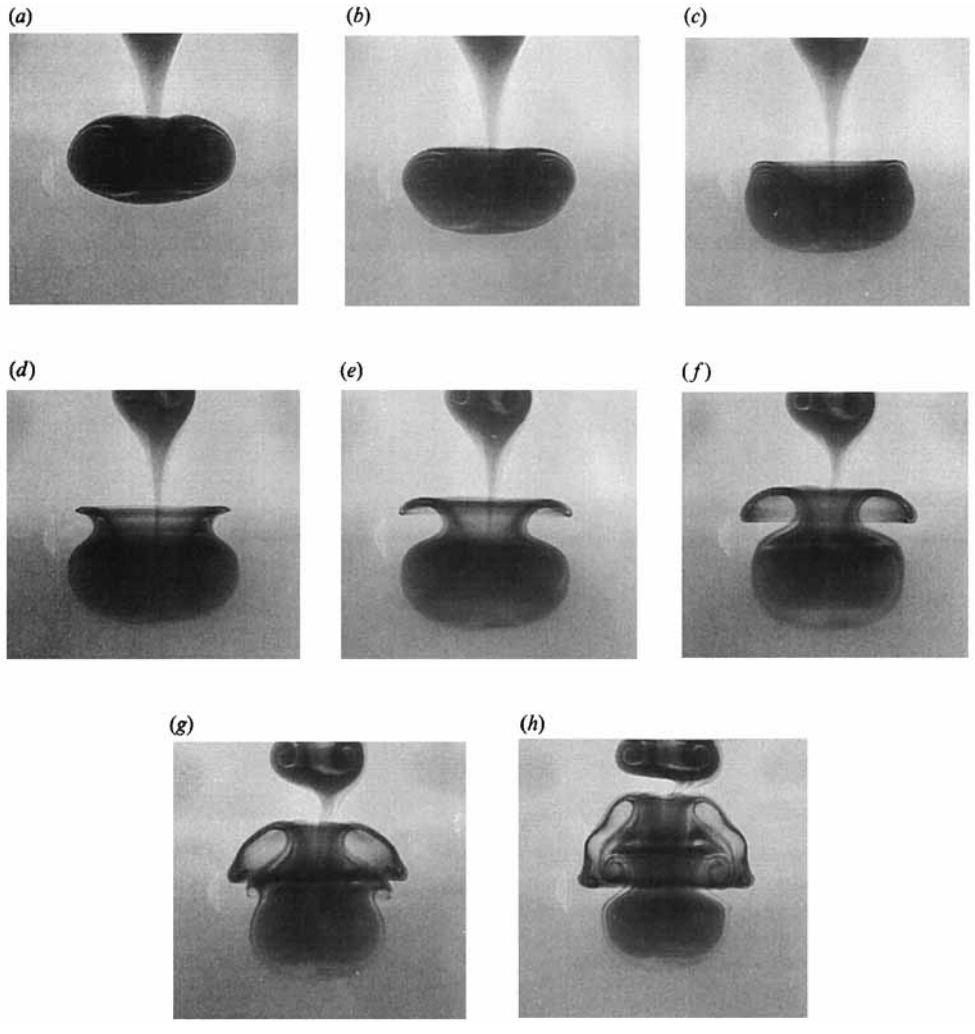

FIGURE 6. Photographic sequence showing vortex ring interaction for $AR = 0.025$ (Case 2 in table 1). For this somewhat larger value of AR, the ring does not penetrate as far through the interface as in figure 5. Notice the formation of secondary vortices as fluid is ejected back by baroclinically generated vorticity and the associated development of an intricate 'crown' structure in the backflow.

Case	ρ_2/ρ_1	Γ	A	R	AR
1	1.0020	92 cm^2/s	0.0010	13.9	0.014
2	1.0100	154 cm^2/s	0.0050	5.0	0.025
3	1.0100	74 cm^2/s	0.0050	21.5	0.108
4	1.0100	22 cm^2/s	0.0050	238.7	1.19
5	1.0025	110 cm^2/s	0.0012	9.7	0.012
6	1.0050	108 cm^2/s	0.0025	10.1	0.025
7	1.0100	74 cm^2/s	0.0050	21.5	0.108
8	1.0100	22 cm^2/s	0.0050	238.7	1.19

TABLE 1. Experimental conditions for figures 5–12.

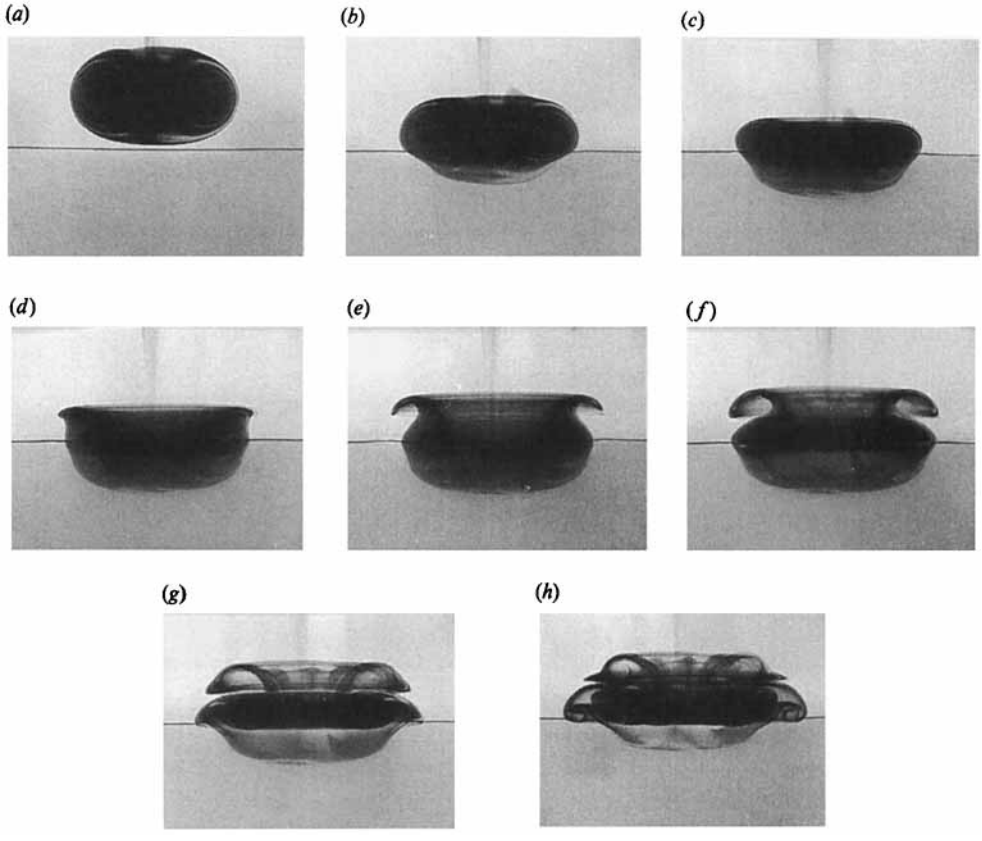

FIGURE 7. Photographic sequence showing vortex ring interaction for $AR = 0.108$ (Case 3 in table 1). For this value of AR the interaction is significantly different from that in figure 6, although there is still some penetration of the interface. Secondary and tertiary rings form from baroclinically generated vorticity, but these now orbit around the original ring. Notice the development of a wavy instability in the secondary ring as it is compressionally strained.

showing results from laboratory experiments for the interaction of a vortex ring with such a density interface are given in figures 5–8, corresponding to the conditions for cases 1–4 listed in Table 1. These span nearly two orders of magnitude in the parameter AR. Cross-sectional photographic sequences showing the internal structure for each of these values of AR, corresponding to the conditions listed for cases 5–8 in table 1, are presented in figures 9–12.

The typical evolution for a relatively small value of AR is shown by the cases in figures 5 and 9. The ring can be seen to penetrate the interface completely, pushing an increasingly thinner layer of light fluid ahead of it near the forward stagnation point. As the interface separating the light and heavy fluids is deformed, the baroclinic mechanism generates vorticity along the interface with a sense that opposes the downward motion of the ring. (This is simply the buoyancy body force seen from the point of view of vorticity.) The opposing action of this interfacial vorticity brings the outermost layer of fluid moving with the ring to rest and expels it back into the light fluid, accompanied by heavy fluid which 'splashes' upwards from the other side of the interface. This in turn brings a fresh layer of ring fluid and heavy fluid into contact at the interface, and in turn continues the baroclinic generation at the interface and subsequent expulsion of the adjacent light and heavy

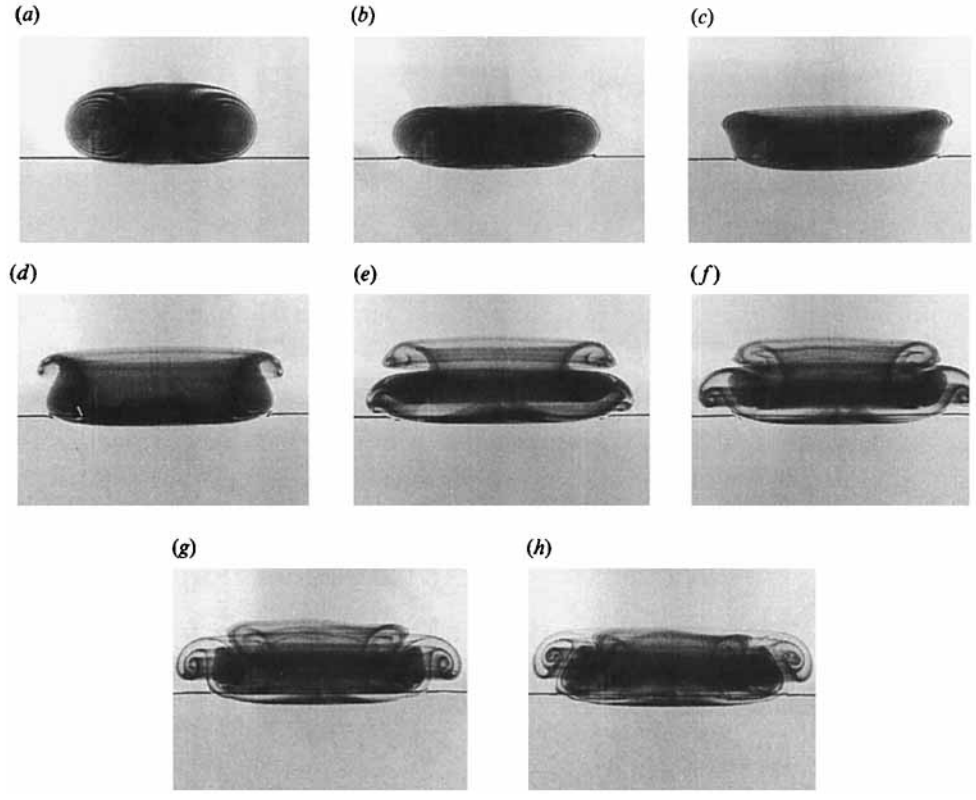

FIGURE 8. Photographic sequence showing vortex ring interaction for $AR = 1.19$ (Case 4 in table 1). Such relatively large values of AR are characterized by essentially no penetration of the vortex through the interface, and the interaction is basically similar to that in figure 7. At this value the transition to this type of interaction is complete; increasing AR even further shows virtually the same interaction. (Note that this sequence has been compressed in time by a factor of two to allow the later stages of development to be shown.) Compare also with figure 26.

fluid layers into the light fluid. Note that, rather than the ring simply rebounding from the interface and more or less retaining its shape, this process by which ring fluid is expelled back into the light fluid may be likened more to peeling back successive layers of an onion. This continues until all of the original ring fluid is ejected back into the light fluid in a thin continuous sheet along with the accompanying heavy fluid. During this process, the vortices themselves are actually pushed towards each other and the vortex speed remains large until the very end, although the amount of downward going fluid becomes less and less. (This is somewhat reminiscent of Maxworthy's (1977) observation of a decrease in size followed by eventual collapse of a turbulent vortex ring moving downward through a weak continuous density gradient.) The interfacial vortical sheet in the backflow forms a jet that is itself Kelvin–Helmholtz unstable and develops wavy instabilities. This can be seen, for example, in figures 6 and 10. These instabilities roll up to form distinct vortical structures, having the opposite sense of circulation as the original ring, which propagate back into the light fluid. The subsequent development of the backflow into largescale Kelvin–Helmholtz 'billows' is clearly visible in these sequences. The combined effect forms a fairly spectacular 'crown' in which the ring fluid, the light fluid and the heavy fluid are all intertwined. Note that many of these

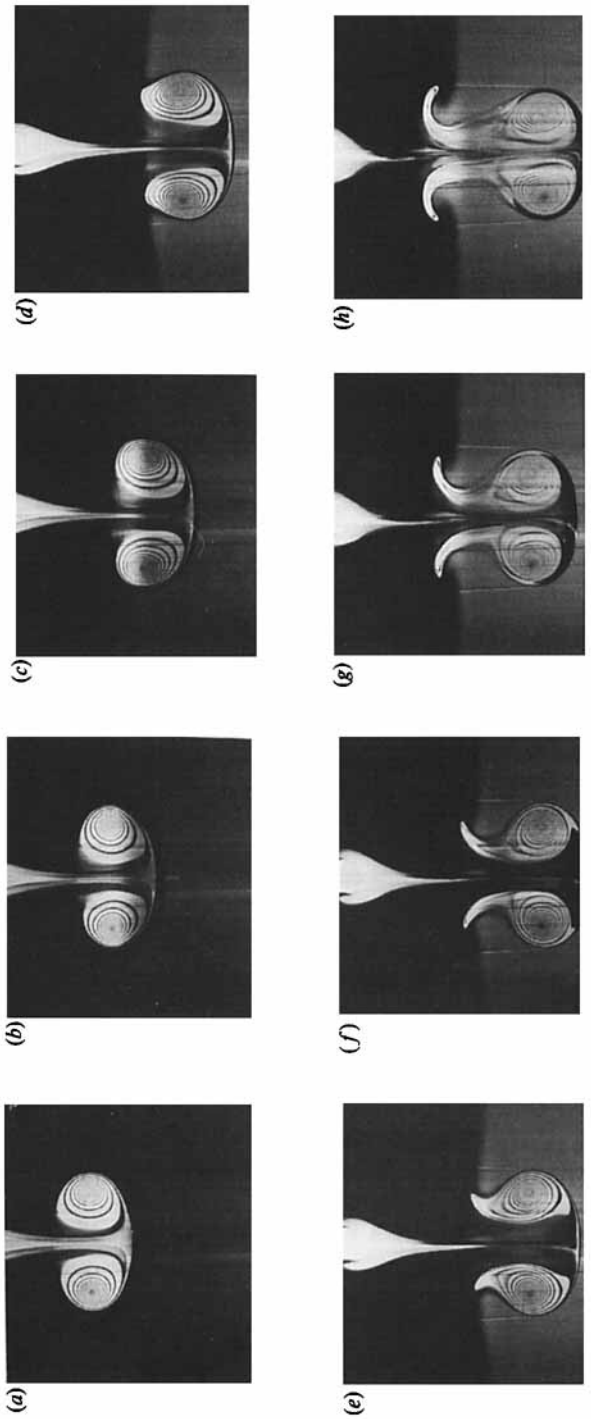

FIGURE 9. Cross-sectional (LIF) photographic sequence showing vortex ring interaction for $AR = 0.014$ (Case 5 in table 1). The internal structure of the interaction can be clearly seen, as well as the deformation of the interface. Notice that a considerable amount of top fluid is carried into the bottom fluid and trapped at the head of the vortex as the cores are pushed together. Compare also with figure 5.

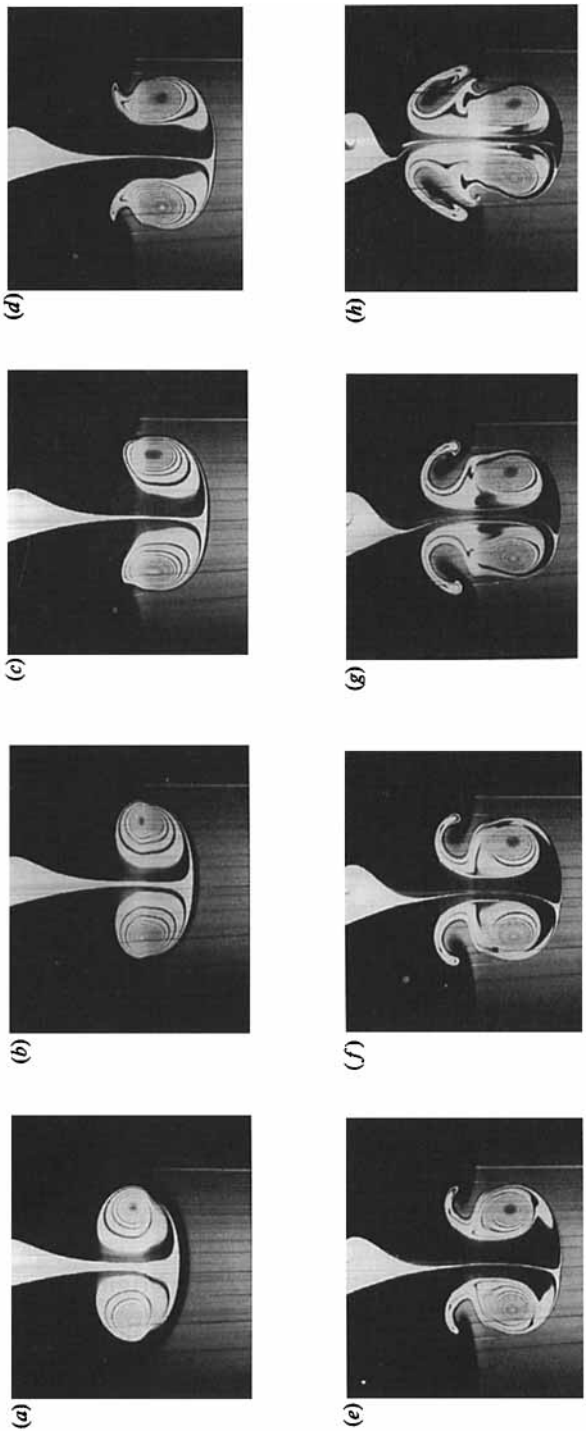

FIGURE 10. Cross-sectional (LIF) photographic sequence showing vortex ring interaction for $AR = 0.025$ (Case 6 in table 1). Note that the backflow 'crown' contains top fluid, bottom fluid and ring fluid intertwined. Notice also the formation of secondary vortices from the Kelvin–Helmholtz instability of the backflow vortex sheet. Compare also with figure 6.

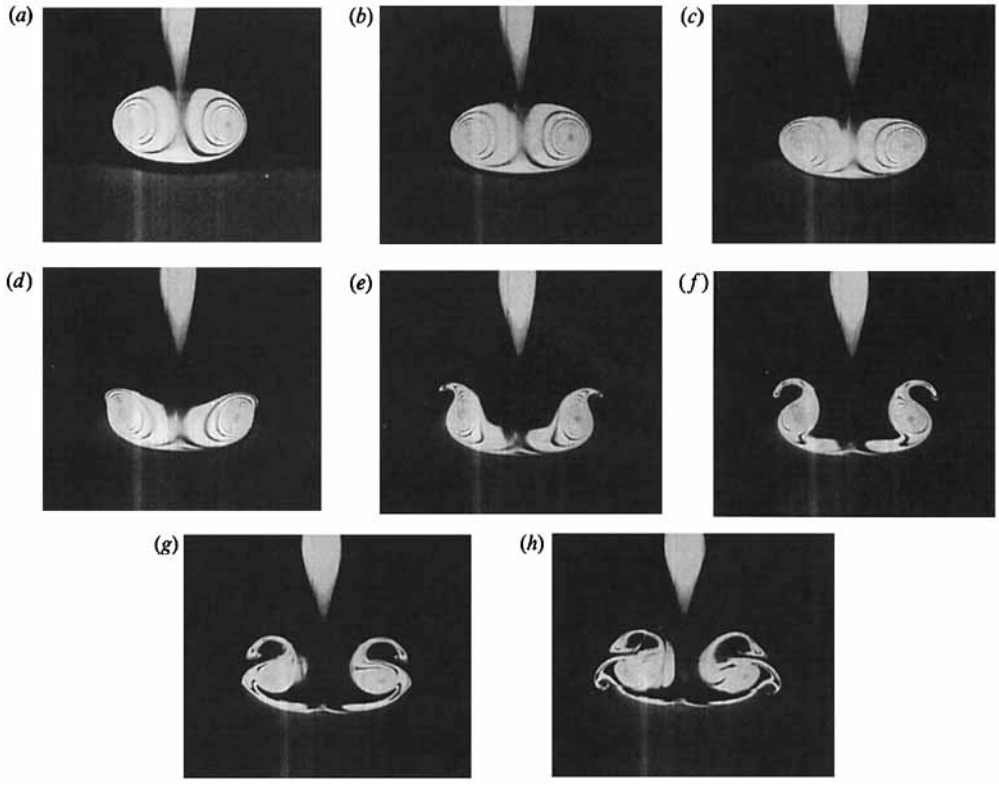

FIGURE 11. Cross-sectional (LIF) photographic sequence showing vortex ring interaction for $AR = 0.108$ (Case 7 in table 1). Notice the formation of secondary and tertiary vortex rings which orbit around the original ring. Compare also with figure 7.

features can be identified in the sequences in figures 5–8 and 9–12 for which the parameter AR is relatively small.

As AR increases, however, the interaction is characterized less and less by this penetration and peeling process and its accompanying crown formation in the resulting backflow. Instead, a distinctly different type of interaction begins to dominate.

The sequences in figures 8 and 12, with $AR = 1.19$, demonstrate the more typical evolution for relatively large values of AR. In such cases, as suggested by the arguments in §2.2, the ring barely penetrates into the heavy fluid and the interface remains nearly flat. The dyed fluid boundary shows that baroclinically generated vorticity with the opposing sense of circulation is swept radially outward along the interface and then up along the sides of the ring. This interfacial vorticity rolls up to form a second axisymmetric vortex ring directly outside and slightly behind the original ring with the opposite sense of circulation as the original ring. Their mutual induction causes the two ring cores to orbit around one another, with the original ring increasing in diameter while the diameter of the secondary ring decreases. As a consequence, the two rings are subjected, respectively, to extensional and compressional straining along their azimuthal directions. The destabilizing effect of the compressional strain eventually leads to the development of a wavy structure in the secondary ring suggestive of a Widnall-like instability (Widnall & Sullivan 1973; Widnall *et al.* 1974) modified here by the presence of azimuthal strain. The onset of

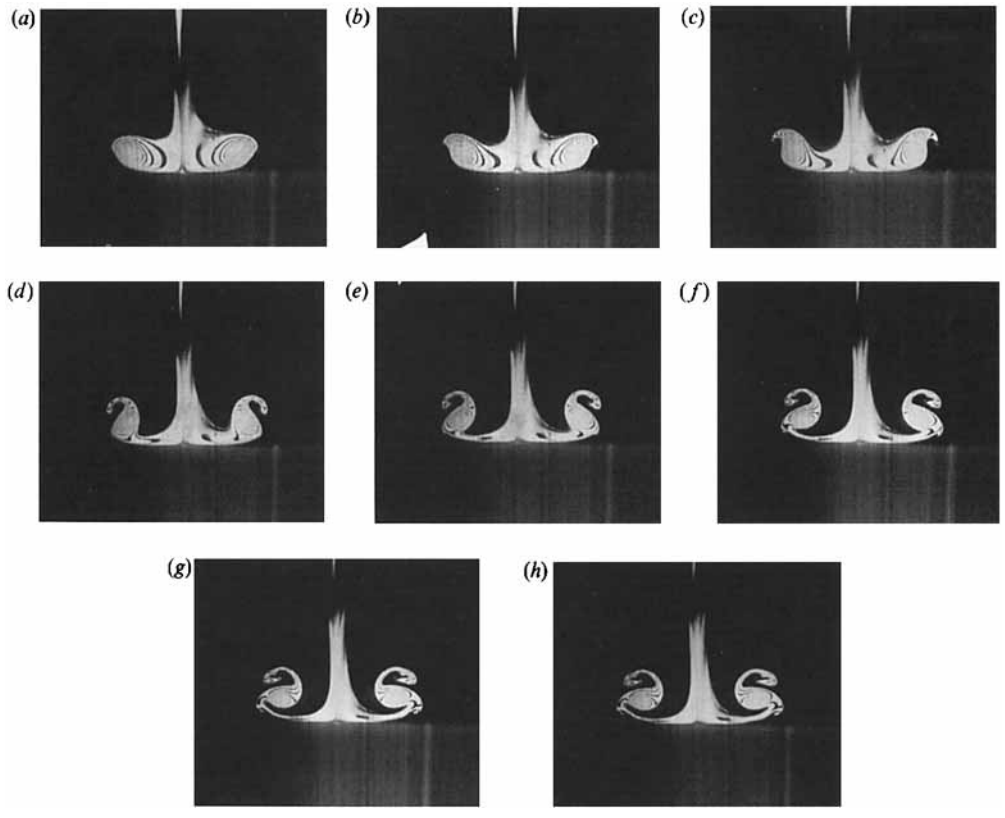

FIGURE 12. Cross-sectional (LIF) photographic sequence showing vortex ring interaction for $AR = 1.19$ (Case 8 in table 1). Although the interface remains nominally flat, baroclinic generation remains present and continues to form secondary and tertiary vortex rings. Compare also with figures 8 and 27.

this instability in the secondary ring exhibits a dependence on the Reynolds number (Γ/ν) of the original ring, though this dependence has not been investigated in any detail here. Such a Reynolds-number effect is, however, consistent with instability observations by Krutzsch (1939) and analyses by Widnall & Sullivan (1973) and Saffman (1978) for individual vortex rings. As a consequence, for describing those aspects of the interaction dynamics associated with this instability, the Reynolds number enters as a second similarity parameter in addition to AR. Note also that the extensional strain in the original vortex ring renders it stable. The amplitude of the secondary ring instability continues to increase while at the same time a third vortex ring is forming from baroclinically generated vorticity carried away from the interface by the original ring. The secondary ring continues to orbit around the original ring and eventually lies completely within it. The instability in the secondary ring develops to quite large amplitude but retains a very nearly periodic structure. The third ring undergoes an evolution very similar to that of the secondary ring. Note that the original ring has remained quite axisymmetric throughout this entire process. In some cases, even a fourth ring can be seen to form from vorticity generated at the interface. Dissipation associated with the diffusion of vorticity slows this process as time progresses, and appears to place a limit on the number of rings that will ultimately form in a given case. Moreover, minute imperfections in the

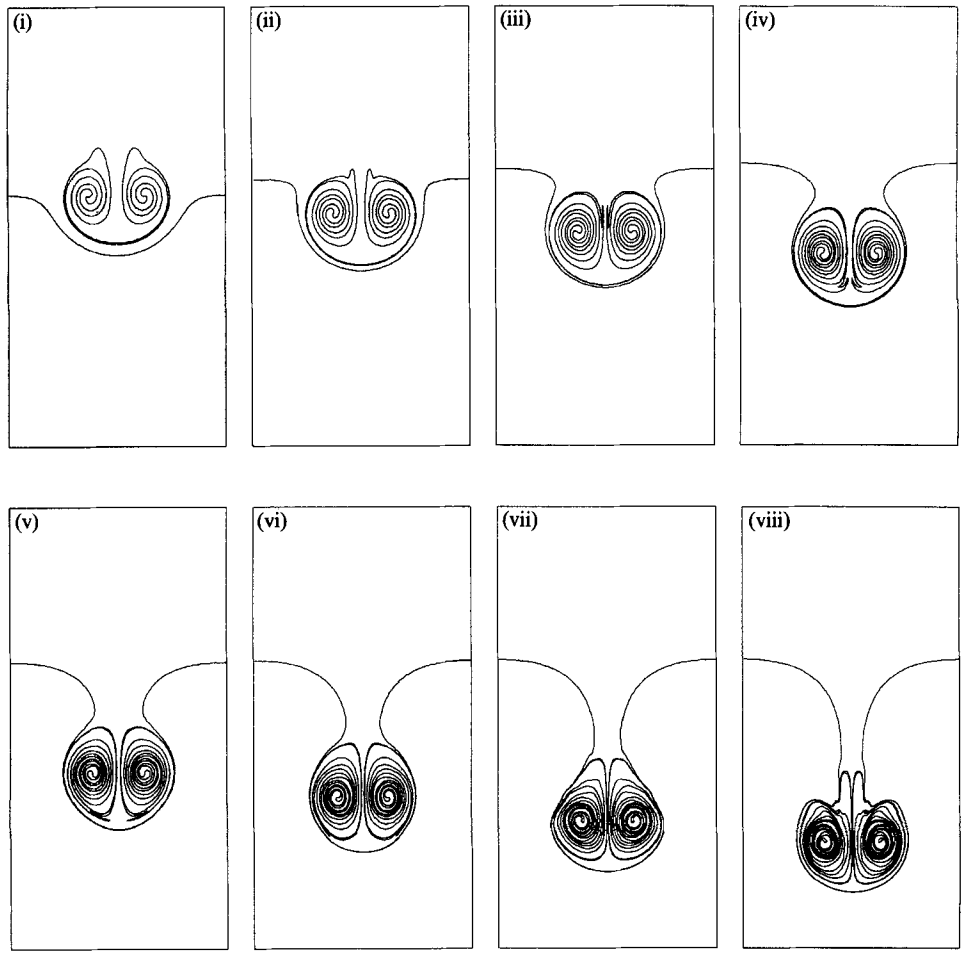

FIGURE 13. Computational sequence showing vortex pair interaction for $AR = 0$. In this case the interface is simply a passive line of markers. The computations use a VIC-based method for stratified flow on a 32×64 grid. The frames shown are at non-dimensional times of (i) $t = 9.0$, (ii) 12.6, (iii) 16.2, (iv) 19.8, (v) 23.4, (vi) 30.6, (vii) 34.2, and (viii) 37.8. The grid and the times shown are the same in figures 13–18.

symmetry can become evident during these very late stages of the interaction, and can grow to eventually destroy the overall symmetry and accelerate the dissipative process.

These two types of interactions appear to be limiting cases for the dynamics of small and large values of AR, respectively. For intermediate values of AR, features of both of these types of interactions can be seen in varying degrees. Note also that the timescale for each of these interactions is observed to correlate well with (a^2/Γ), as presumed by the similarity arguments in §2. For example, the differing circulations for cases 1 and 5 should render the duration of the interaction in figure 5 longer than that in figure 9 by the factor 1.20. Indeed, the five time intervals between figures 5(*c*) and 5(*h*) correspond roughly to the four intervals between figures 9(*d*) and 9(*h*). On the other hand, the interaction in figure 6 should occur on a timescale shorter than

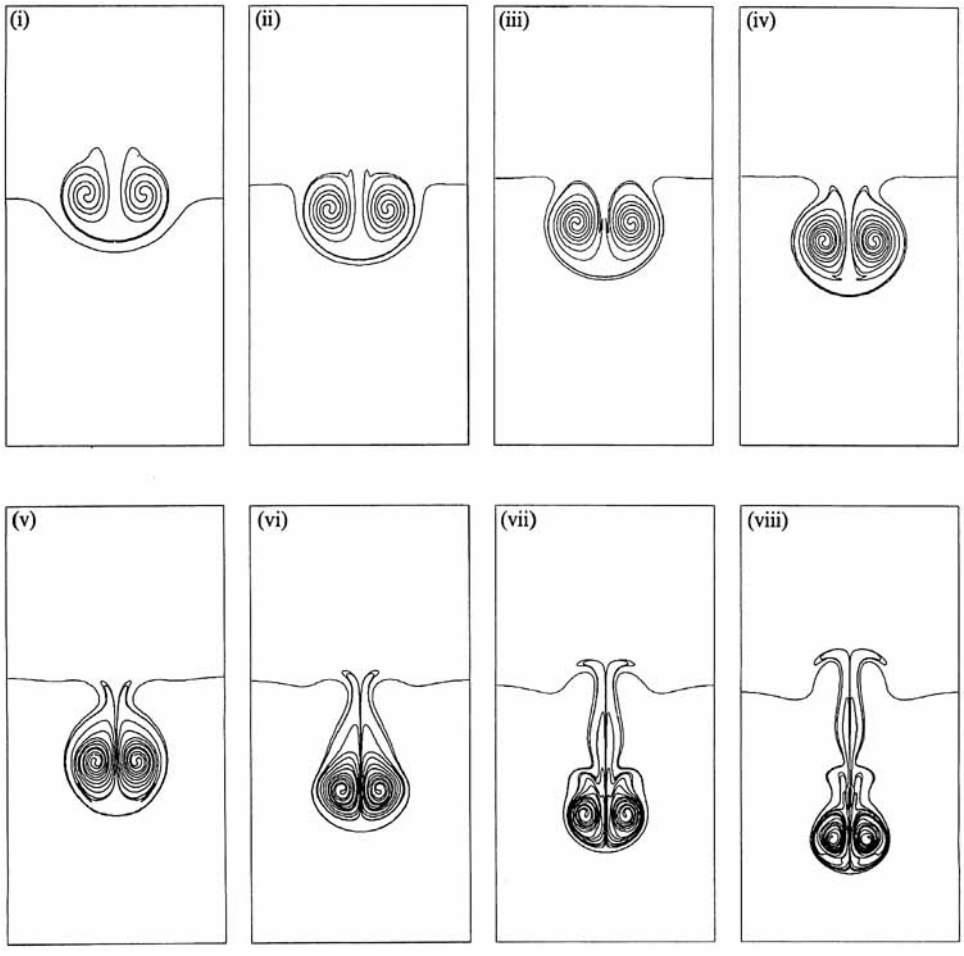

FIGURE 14. Computational sequence showing vortex pair interaction for $AR = 0.005$, corresponding to a relatively strong vortex encountering a relatively weak interface.

that in figure 10 by the factor 0.70, and in this case the four time intervals in figures 6(*c*)–6(*g*) correspond approximately to the five intervals between figures 10(*c*) and 10(*h*). More accurate comparisons afforded by cine photography verify this timescaling to greater precision.

The sequences in figures 13–18 show results from inviscid numerical simulations for the interaction of a planar vortex pair with a thin density interface. We begin with the sequence in figure 13, in which $AR = 0$ so that there is no density jump across the interface. The interface is therefore just a passive line of markers and has no dynamical significance whatsoever for the evolution. As we expect, after the vortex sheet has rolled up, the vortex pair propagates through the interface with constant speed and separation. The separation is about what the simple arguments in §3.2 had suggested, but the speed is somewhat smaller. This is to be expected, since

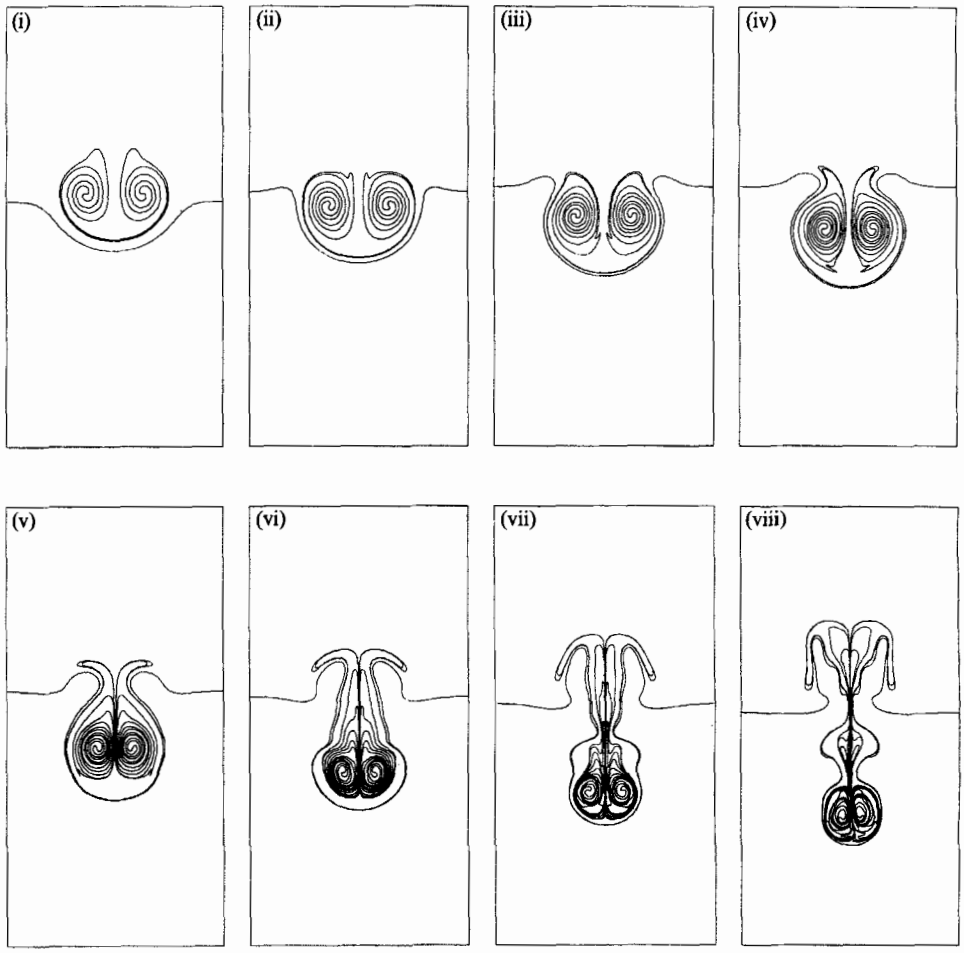

FIGURE 15. Computational sequence showing vortex pair interaction for $AR = 0.01$, corresponding to a slightly weaker vortex or slightly stronger interface than in figure 14. Compare also with figures 5 and 9, showing experimental results for vortex ring interaction.

both the finite area of the resulting vortex and the sides of the periodic box affect the motion in this way. In the last frame of this sequence the back side of the vortex has shed some fluid, presumably owing to the fact that the rear stagnation point has converging streamlines and is therefore unstable to small perturbations.

For the sequences shown in figures 14–18, the value of AR increases successively from 0.005 to 0.1. Perhaps the most striking feature evident in this succession is that the resulting interaction dynamics show a remarkable similarity to those observed in the laboratory experiments for vortex rings. This is true despite the rather obvious differences between these planar vortex pairs and the axisymmetric vortex rings, and the further difference that these simulations are inviscid. Of course, numerical differences in the precise value of AR associated with any particular set of interaction dynamics are to be expected.

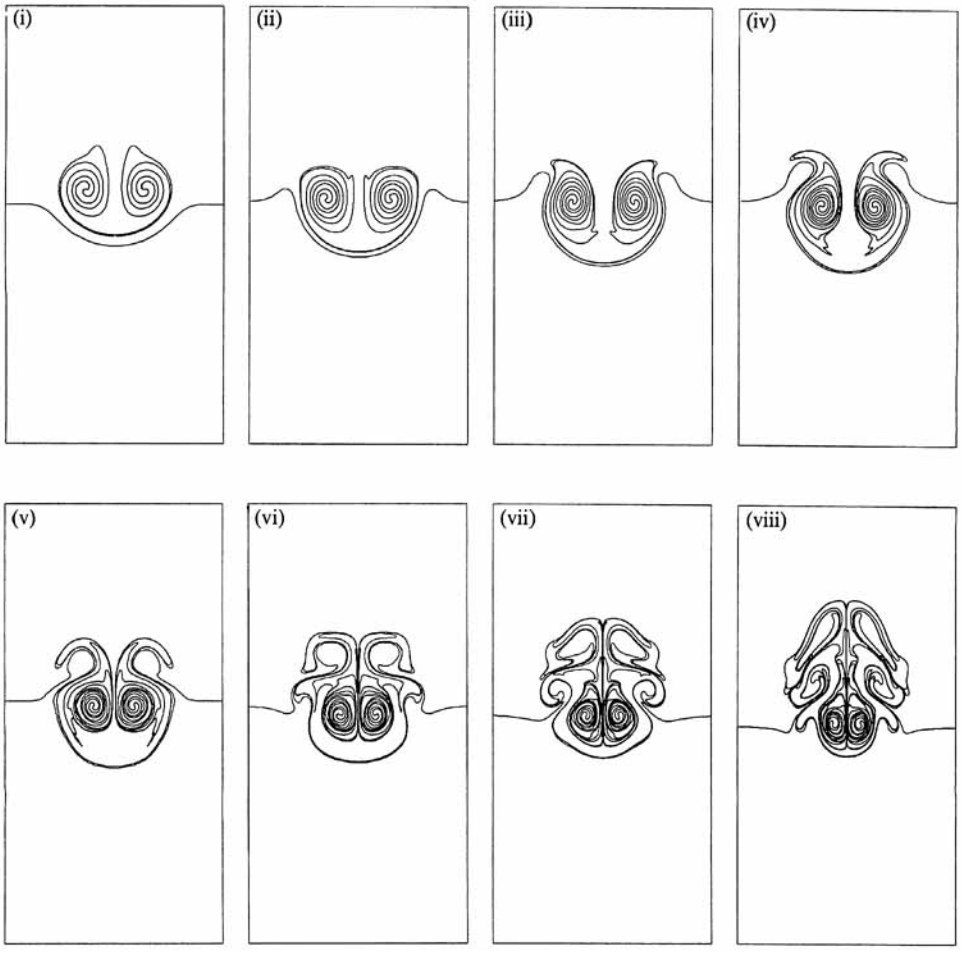

FIGURE 16. Computational sequence showing vortex pair interaction for $AR = 0.02$. The vortex is somewhat weaker, or the interface somewhat stronger, than in figure 15. Compare also with figures 6 and 10.

The simulations show that, for relatively small values of AR, the vortex centres move closer together as the vortex penetrates the interface, and the vortex speed remains nearly constant as indicated in figure 19, where we show the depth of penetration versus time. This is presumably due, in part, to the fact that although the baroclinic vorticity along the interface will counteract the downward motion, it also pushes the vortices closer together and their mutual interaction is therefore stronger. The actual amount of fluid that continues to move with the vortex decreases with time as fluid carried by the vortex is pushed back by baroclinically generated vorticity on the interface. In this way, the vortex pair is stripped of its accompanying relatively low vorticity fluid as it propagates downward. This fluid is ejected back toward the light fluid. Heavy fluid also splashes upward as a result of vorticity in the backflow. This backflow forms a two-dimensional jet which is

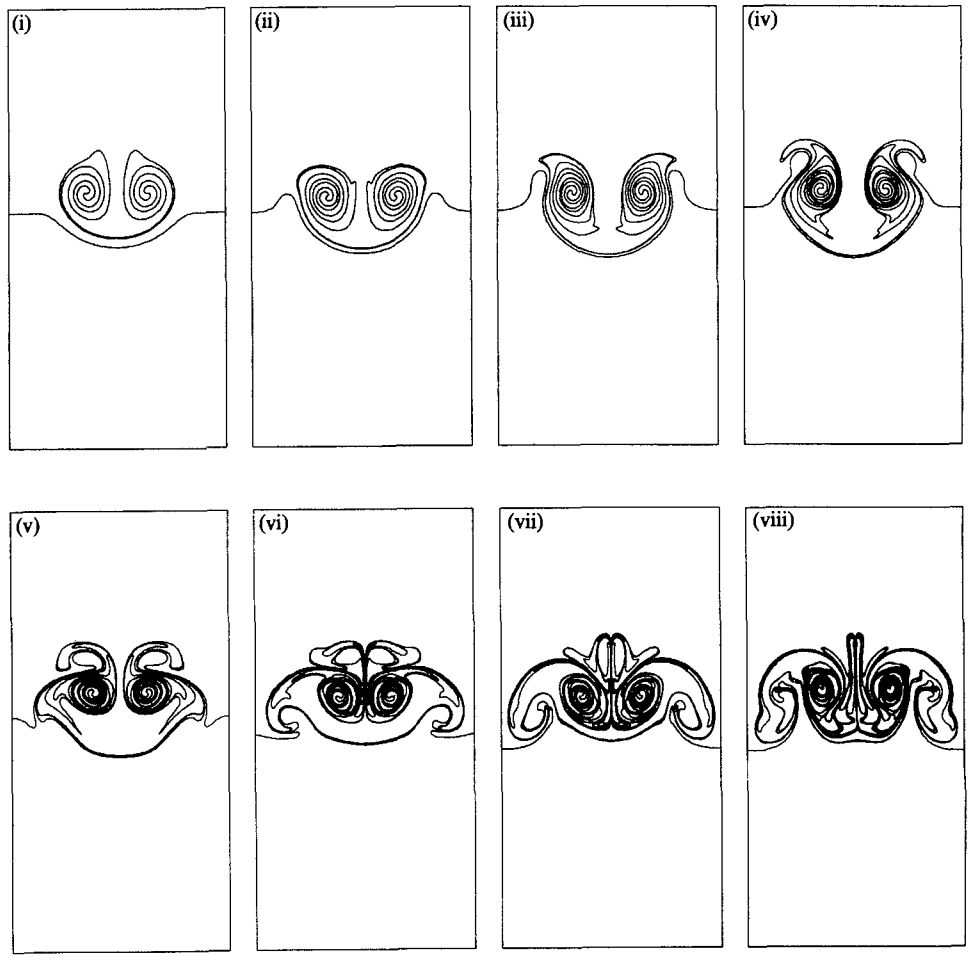

FIGURE 17. Computational sequence showing vortex pair interaction for $AR = 0.03$, corresponding to a comparatively weaker vortex encountering a comparatively stronger interface than in figure 16. Compare also with figures 7 and 11.

Kelvin–Helmholtz unstable, much as was seen for the axisymmetric case. As this backflow jet enters the region occupied by the light fluid it is pushed sideways by the baroclinic vorticity, forming large vortical structures with the opposing sense of circulation to the original vortex pair, which then propagate upwards into the light fluid. As AR is gradually increased, the evolution is similar although the original vortex pair loses accompanying fluid faster and the Kelvin–Helmholtz instability of the backflow jet develops more rapidly. As a result there is more fluid in the crown over the time span shown here, and the heavier fluid has splashed higher.

Once AR becomes relatively large, a major difference in the evolution is that the downward motion of the vortices is stopped about when they are at the interface, as was also seen for the vortex rings. For example, in figures 16 and 17 the fluid carried with the vortices still penetrates the heavier fluid somewhat and is then thrown back,

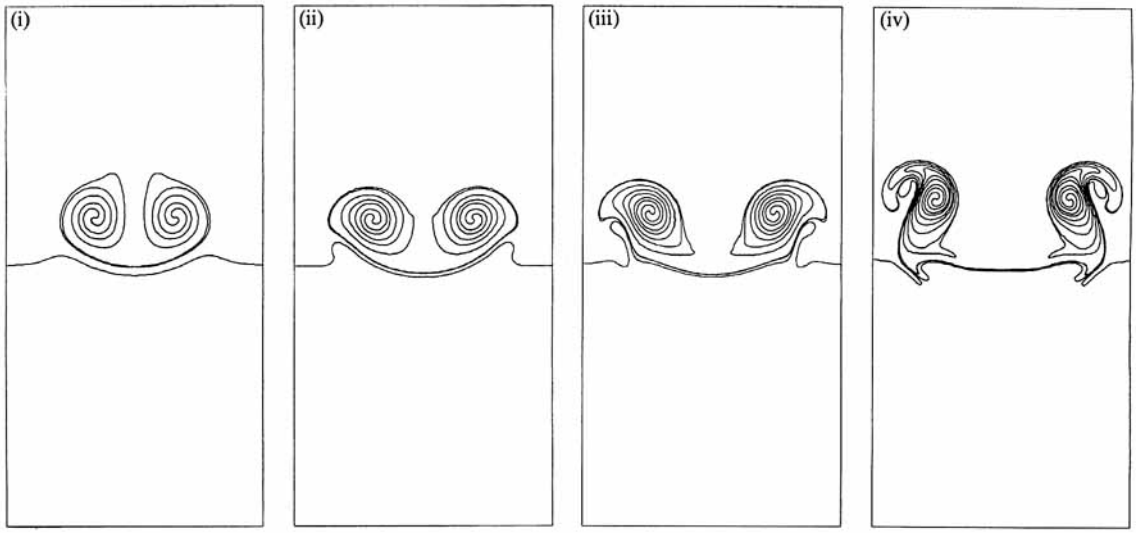

FIGURE 18. Computational sequence showing vortex pair interaction for $AR = 0.10$. In this case, the vortex barely penetrates the interface. Compare also with figures 8 and 12. Note that only the first four times are shown. The longer time development for a larger computational box is shown in figure 27.

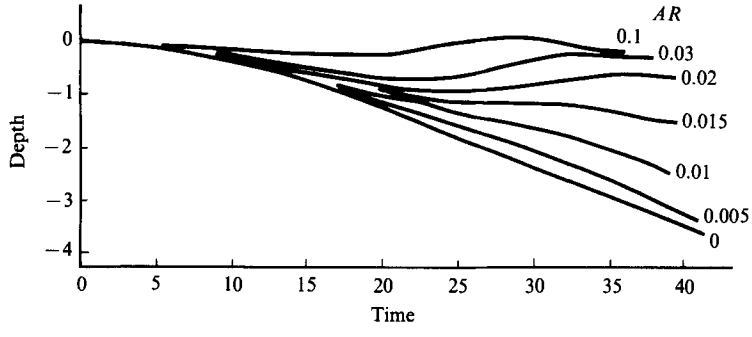

FIGURE 19. Dimensionless penetration depth (centreline displacement of interface) versus dimensionless time from the numerical simulations in figures 13–18. Notice that for $AR < 0.01$ the vortices penetrate deep into the bottom fluid, while for $AR > 0.02$ there is very little penetration.

but in figure 18 there is no longer any penetration to speak of. This can be quantitatively seen in figure 19 and in somewhat different form in figure 20, where we show the penetration depth as a function of AR for two different values of the non-dimensional time obtained from these simulations. These results reinforce our notion of a transition from one characteristic set of interaction dynamics to another as AR increases. Note that for $AR < 0.01$, the vortices propagate through the interface and their speed is not significantly reduced over the time span of the simulation, while for $AR > 0.02$, there is little penetration of the interface. The $AR = 0.015$ case, shown in detail in figure 21, lies right in the transition range. In this case, at about $t = 27$, the downmost part of the penetration is formed by light fluid carried along in front of the vortex pair. As time progresses, the interfacial vorticity strips this fluid away and ejects it back into the light fluid, thus slowing the rate of penetration for this value of AR in figure 20. At larger times, however, the vortex

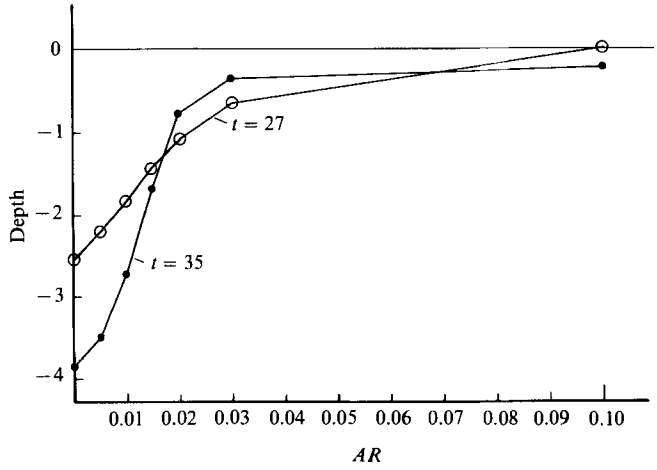

FIGURE 20. Penetration depth versus similarity parameter AR at two different dimensionless times. Notice the relatively sharp transition from strong dependence on AR to relatively weak dependence.

pair can be seen in figure 21 to catch up with the interface and again increases the rate of penetration, as evidenced in figure 20. For even larger values of AR, as in figures 17 and 18, the original vortices now separate slightly and two distinctly different sets of secondary vortices form. The first set is similar to the ones in figure 16 to the extent that they form above the original vortex pair, but the second set forms below the original pair and is then lifted up outside the original pair at the same time as the first set is drawn down between the original vortices. As a result, there is no significant crown formation in figure 17. In figure 18, this transition is essentially completed. The original vortex pair separates as it hits the interface and the secondary vortices form below the original pair and orbit around them, eventually being drawn down between them. The evolution for large AR is also quite similar to that observed experimentally for vortex rings in figure 5–12.

4.3. *Effects of computational boundaries*

It is worth commenting at this point that the width of the periodic computational box in figures 17 and 18 appears rather narrow in comparison with the lateral extent of the interaction. Although such periodic boundaries simulate the influence of straight sidewalls on the interaction, the principal interest here is in studying the interaction in an essentially unbounded domain. This suggests that the computations might no longer accurately simulate the interaction in an infinite space, since the primary vortices might be significantly influenced by their counterparts in the next period and thereby lifted upward and away from the interface to a greater extent than in an infinite domain. Note that the present choice of box size is largely a matter of convenience, since the resulting computations proceed much faster than if a large amount of relatively inactive fluid were included. It is therefore of interest to examine the extent to which the results change as the width of the computational domain is increased.

Figure 22 compares the large-amplitude stage of the interaction for $AR = 0.015$, shown previously in figure 21, with another simulation having the same AR and identical initial conditions but with a computational box twice as wide. The principal apparent difference is that, as expected, the interface everywhere outside the region

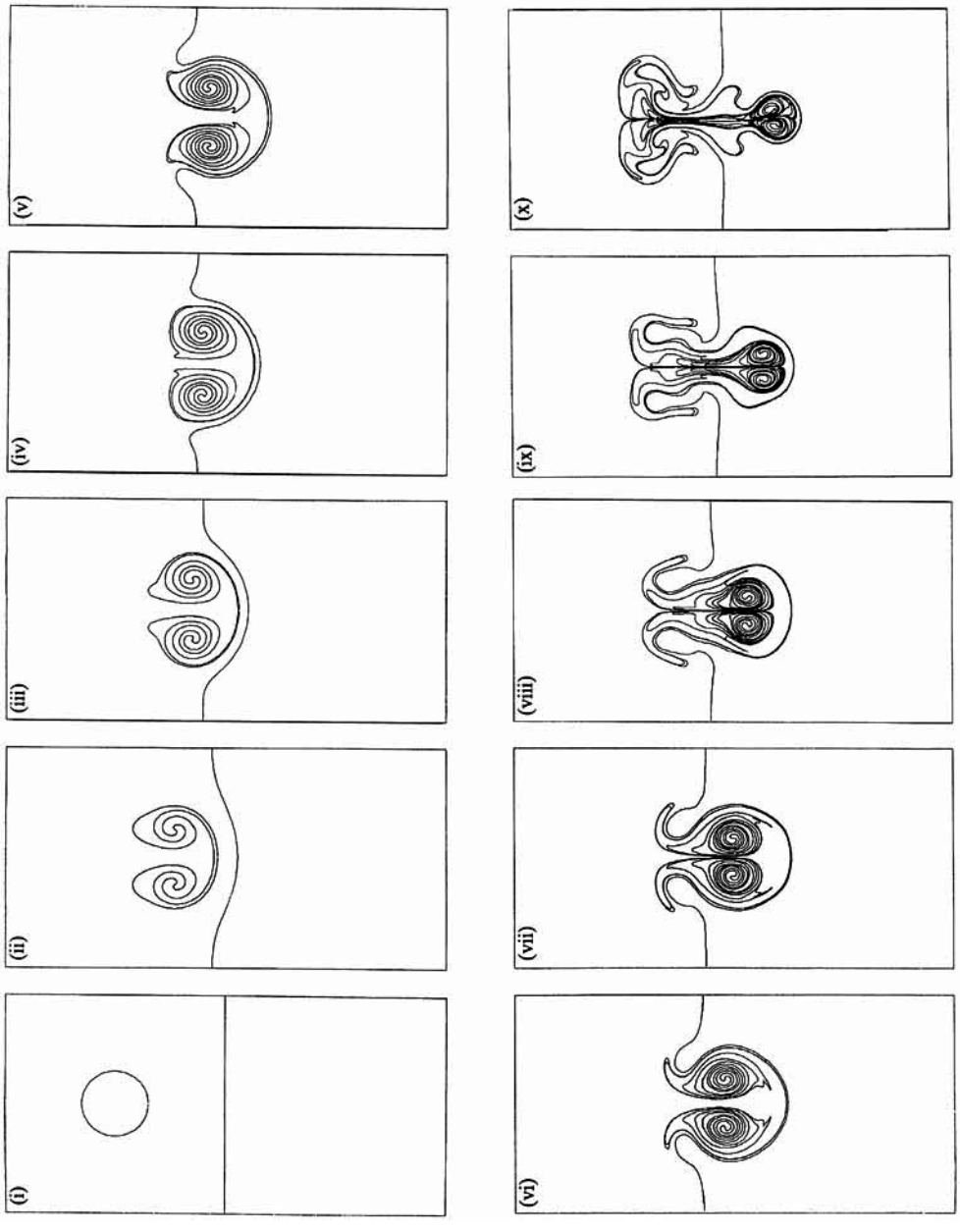

FIGURE 21. Computational sequence showing vortex pair interaction in the transition regime, $AR = 0.015$. The vortex partly penetrates through the interface and is then slowed down by baroclinically generated vorticity that 'peels' away some of the accompanying fluid. The 'crown' formation is quite pronounced for this case.

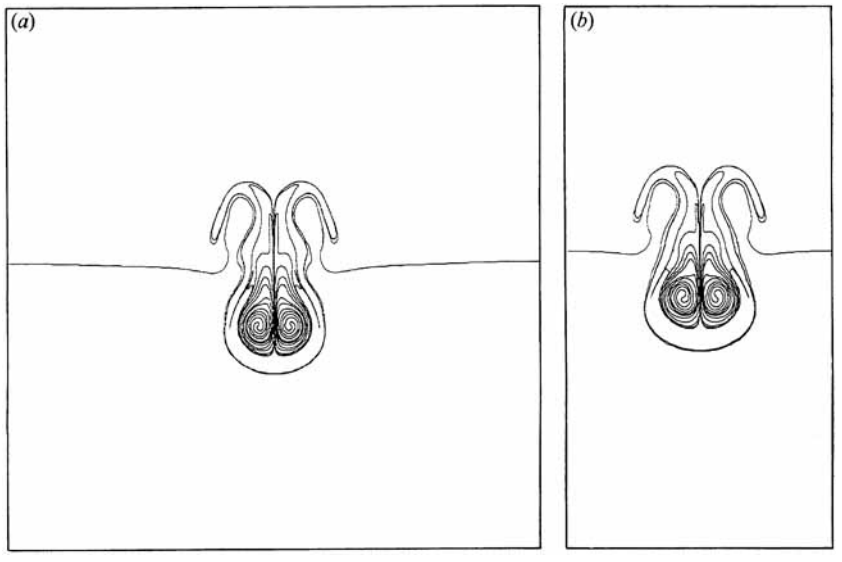

FIGURE 22. Effect of periodic box width on computed vortex pair interaction for $AR = 0.015$. (*a*) wider box; (*b*) narrow box. Notice that, as expected, the vertical displacement of the interface due to the 'crater' formed by the vortex is more pronounced in the narrow box. Otherwise, the effects of box size are minimal.

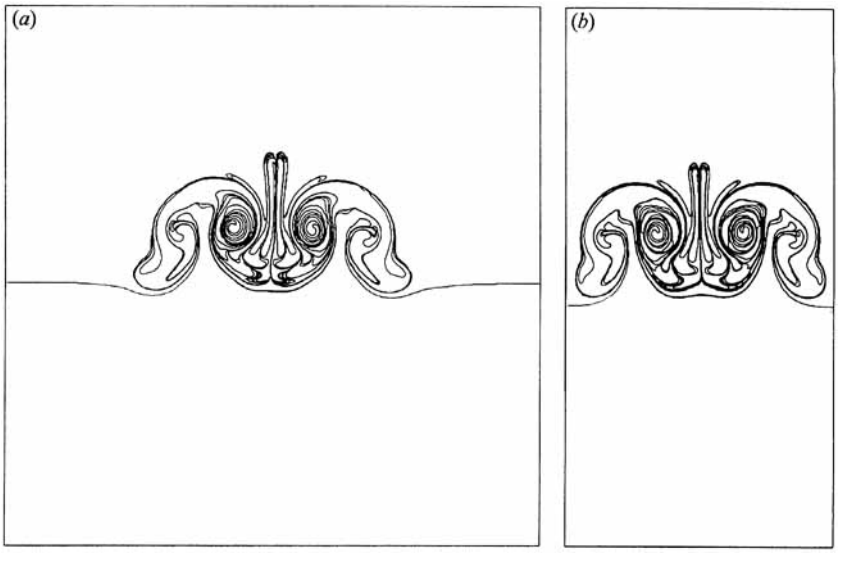

FIGURE 23. Effect of periodic box width on vortex pair interaction for $AR = 0.03$. (*a*) Wider box; (*b*) narrow box. The overall spreading of the 'crown' is slightly larger in the wider box, but even in this extreme case the effects of the box size are minimal.

of interaction has been raised by the displacement effect of the penetration 'crater'. However, the penetration depth relative to the interface is the same in both cases. Moreover, this displacement effect would vanish as the penetration depth goes to zero for large AR. A similar comparison at later time for $AR = 0.03$, shown previously in figure 17, is given in figure 23. Again there is very little apparent difference between the two cases. This is true despite the fact that the backflow

almost reaches the sides of the narrower box, and can be attributed to the relatively small circulation associated with the backflow. There are, however, some slight differences discernible. For example, the lateral extent of the vortex system is somewhat smaller. However, even in this extreme case, the minor differences discernible between the results obtained in the narrow and wide boxes are indeed small in comparison with the very large differences apparent among the results for differing values of AR in figures 13–18. We can conclude from this that, in all of these cases, our relatively narrow computational box correctly captures the main features of the interaction dynamics in an infinite domain.

4.4. *Resolution effects*

It is also appropriate at this point to examine the dependence of the numerical simulations on the computational mesh size. In many problems commonly solved by a discrete approximation method, the evaluation of accuracy by grid refinements is a relatively straightforward process. However, additional complications arise when an inviscid model is used to simulate a highly unstable process. In its purest form, an inviscid model is scale invariant and simple scaling shows that a small disturbance will have a growth rate that increases with its wavenumber. This short-scale instability, and its affect on the development of small-scale motions, will be strongly affected by any stabilizing mechanisms introduced in the computational method. As a result, the relevance of any simulation involving such a stabilizing mechanism depends on the extent to which the precise structure of the small-scale motions influences the global solution. Generally, a change in the small-scale stabilization mechanism produces two effects. First, for the roll-up of vortical structures, both the number of turns and the 'fineness' of the roll-up increase as the scale of the regularization in the numerical method is decreased. The convergence of simulations for a single vortex roll-up as the regularization scale is reduced is relatively well understood for vortex blob methods (Krasny 1986) and for the present vortex-in-cell method (e.g. Tryggvason 1988*b*). Secondly, for highly unstable parts of the interface, as the regularization scale is decreased the wavelength of small-scale instabilities also decreases. The second effect is potentially more troublesome, although in the case of Kelvin–Helmholtz instability small-scale instabilities usually amalgamate to form a resulting large-scale structure quite similar to that which would have formed from an initially longer-wave instability. However, sometimes such short-scale instabilities are an entirely different solution branch, triggered by round-off errors (Krasny 1986) and should therefore be eliminated in convergence studies, whereas in other cases it appears natural to expect instabilities of as high a wavenumber as the small-scale regularization will allow.

To investigate the effects of grid refinements on our results, we performed simulations with $AR = 0.03$ and the same initial conditions on a 32^2 mesh and on a 64^2 mesh. The results are compared in figure 24, where the non-dimensional times are approximately the same for each pair of frames. Note that the large-scale features are quite similar. As is to be expected with increasing time, differences in the development of small-scale features become more apparent. The principal effect of the refined grid is to increase the amount of roll-up in the vortex centre. The subsequent motion of the vortex pair as well as the deformation of the interface and the basic pattern of the backflow are much less affected. The major differences lie in the higher growth rates for the Kelvin–Helmholtz instability in the backflow, which lead to earlier roll-up of vortex structures as well as the development of finer scales in the backflow, which have not developed on the coarser grid. Nevertheless, even at

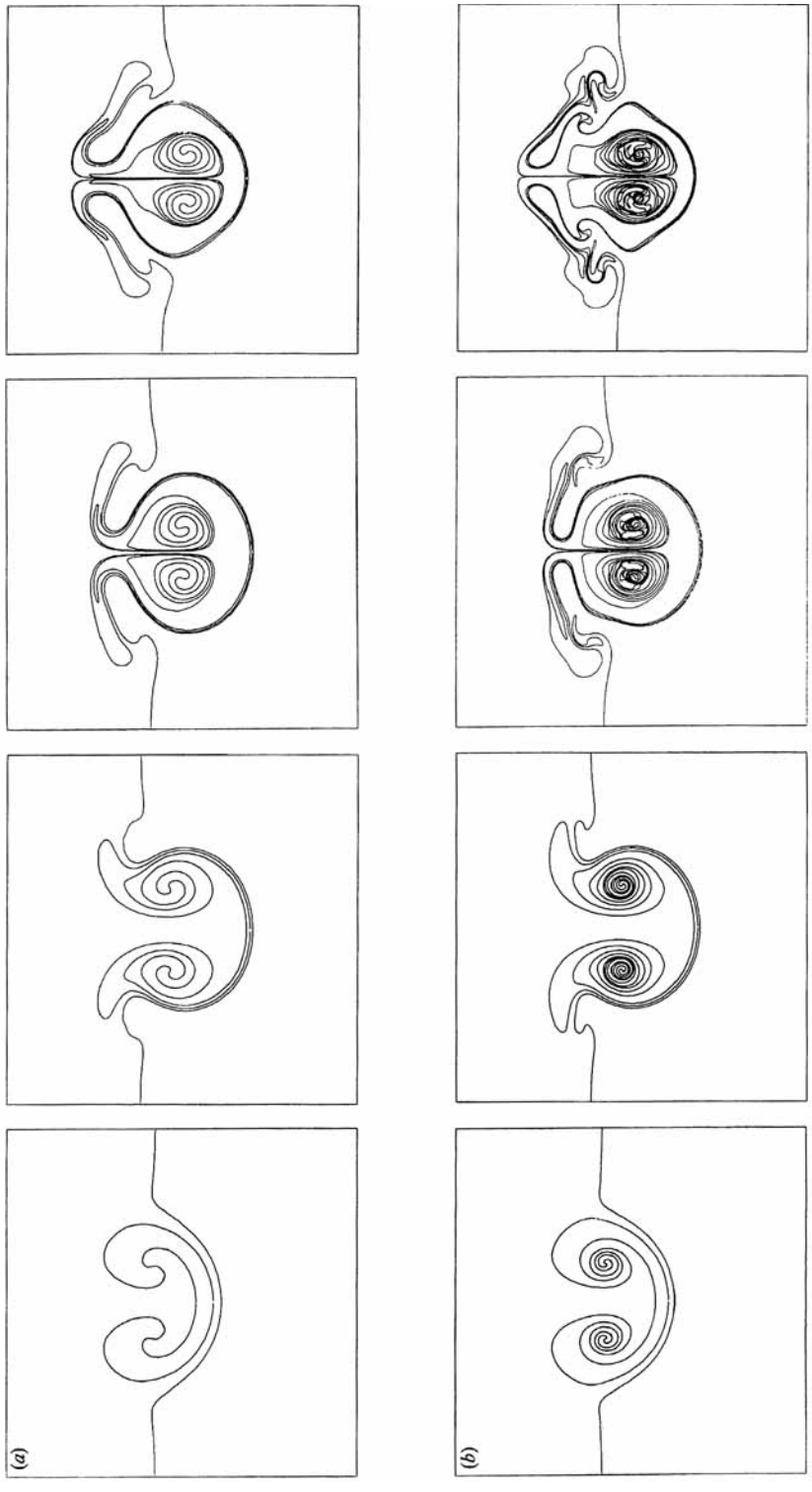

FIGURE 24. Effect of resolution on computed vortex pair interaction for $AR = 0.03$. (*a*) 32^2 computational mesh; (*b*) 64^2 computational mesh. The vortex rolls up more on the finer grid and new small scale structure appears, but the large scale motion is minimally affected.

the longest time shown, the differences discernible are quite small in contrast to those apparent from a comparison in figures 13–18 among differing values of AR. We can conclude that the large-scale features in these numerical calculations appear to simulate accurately the interaction dynamics and will not change appreciably with further grid refinements. However, there are at least some fine-scale details of the simulations that must be viewed as being specific to the particular choice of grid size used here.

4.5. *Effects of core structure*

The initial condition for all the numerical simulations described so far were taken, more or less arbitrarily, as described in §3.2. This study has not addressed the effects of the initial condition on details of the roll-up process, and in general it is not known how the structure of the resulting vortex depends on the initial vorticity distribution. However, since for a fixed circulation the kinetic energy of a vortex depends on its core diameter, and the interactions studied here involve an interchange of kinetic and potential energy, we expect that the core size and structure may have some effect on the interaction. Since the effective core size may vary according to the way in which the vortex pair was generated, it is of some importance to understand the sensitivity of the solution to changes in the core size.

The interaction for $AR = 0.015$, shown previously in figure 21, is shown at the same times in figure 25 for vortices with uniform vorticity cores, called Finite Area Vortex Regions (FAVR) by Zabusky (e.g. Deem & Zabusky 1978). The initial core diameter is $0.42a$ in figure 25(a) and $0.85a$ in figure 25(b). Note that the development in the first frame is nearly the same in both cases, and is quite similar to the corresponding frame in figure 21. However, at later times there are significant differences. For example, in figure 25(a), where the core diameter is small, none of the vortical fluid is torn away from the vortex pair after it penetrates through the interface. As a result the circulation remains large and, as the cores are pushed together, their speed and depth of penetration becomes large. This suggests that for zero core size, or point vortices, the vortices may eventually come arbitrarily close together and thus reach arbitrarily high velocities. Whether such a singularity will appear in a finite time is not known. On the other hand, for the larger core size in figure 25(b), the evolution is quite different and remains more like that in figure 21. A significant amount of the vortical fluid is stripped away from the vortex pair and ejected back, thus reducing the circulation of the remaining downward-moving vortex. The development of the backflow jet also more nearly resembles that in figure 21.

These results demonstrate that the core size of the vortices can have a significant influence on the evolution. However, further calculations show that varying AR for a given core size still leads to a transition between two limiting types of interactions for small and large values of AR.

4.6. *Interaction dynamics in the limit* $AR \to \infty$

The observation in §4.2 that for large values of AR, as shown in figures 8 and 12 and in figure 18, the vortex barely penetrates the interface suggests that under these conditions the interface acts somewhat like an immovable boundary to the vortex. Indeed, as $AR \to \infty$ the velocity component normal to the interface must be zero owing to the interface remaining nominally flat (i.e. $\hat{\boldsymbol{n}} \times \hat{\boldsymbol{j}} \to 0$ in (8) while $AR\,\hat{\boldsymbol{n}} \times \hat{\boldsymbol{j}} \to$ constant, as discussed in §2.2). This motivated us to examine the interaction of a vortex ring with a solid wall. The resulting interaction dynamics are shown in the sequence in figure 26. In this case, the ring circulation is 74 cm^2/s and

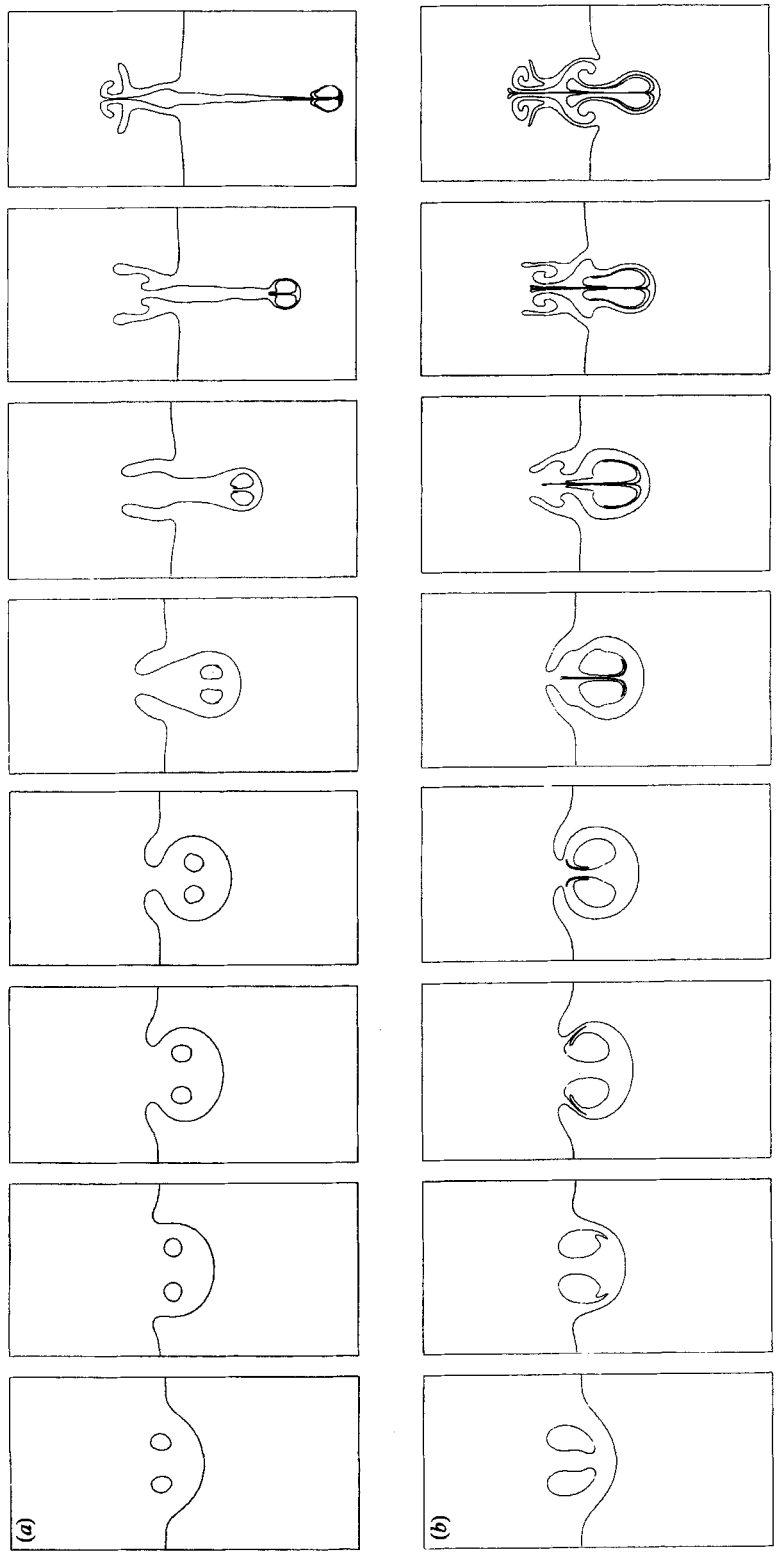

FIGURE 25. Effect of core radius on computed vortex pair interaction for $AR = 0.015$. (*a*) Core radius = $0.42a$; (*b*) core radius = $0.85a$. The vortex pair with the smaller core penetrates much further than for the larger core size. Notice also that some of the vortical fluid has been stripped away from the large cored vortex, but this has not occurred for the smaller core size.

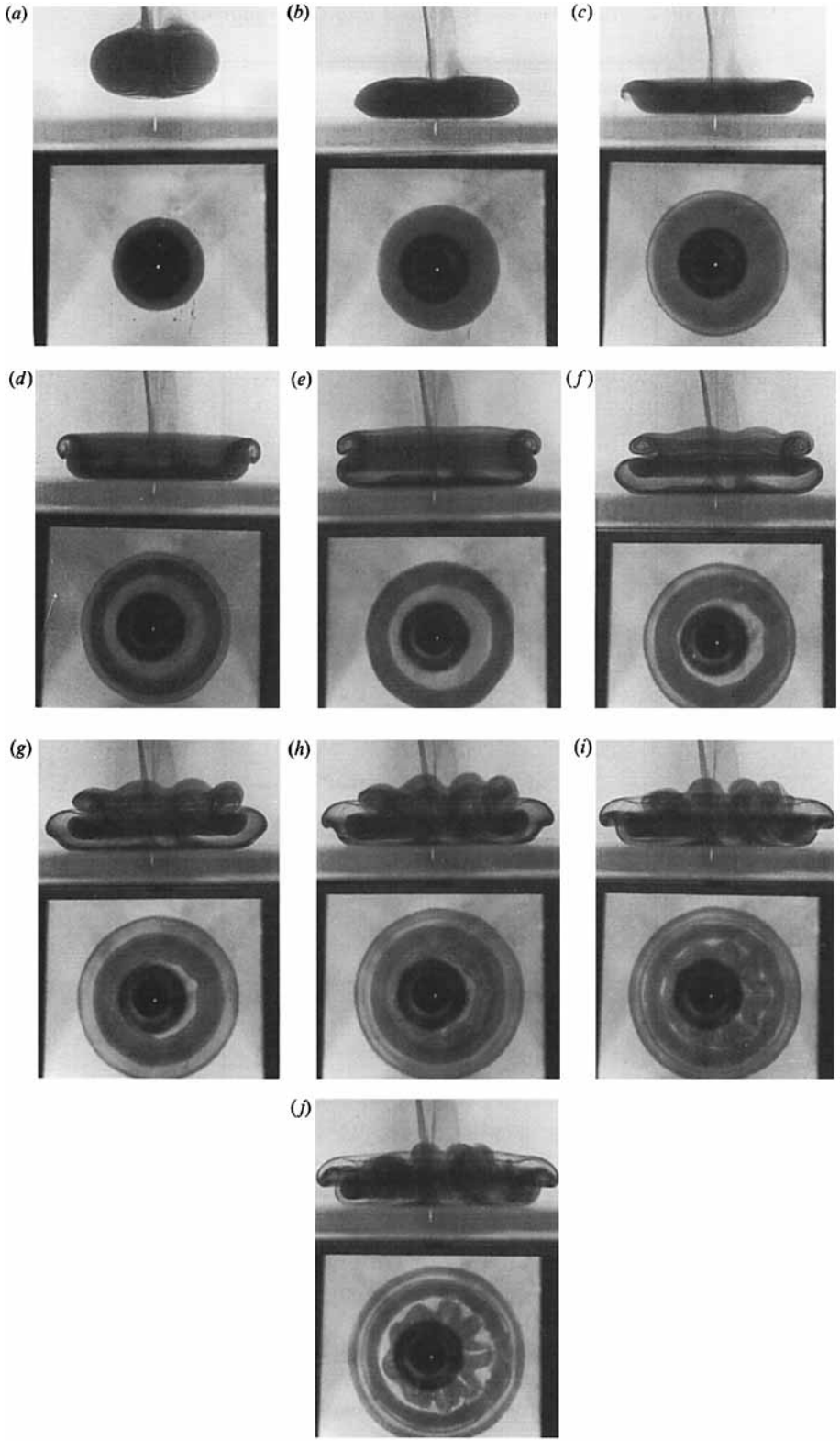

FIGURE 26. Photographic sequence showing the interaction of a vortex ring with a solid wall, giving simultaneous side and bottom views. Although the timescales are different, notice the similarity with the interaction at a density interface for large AR shown in figure 8.

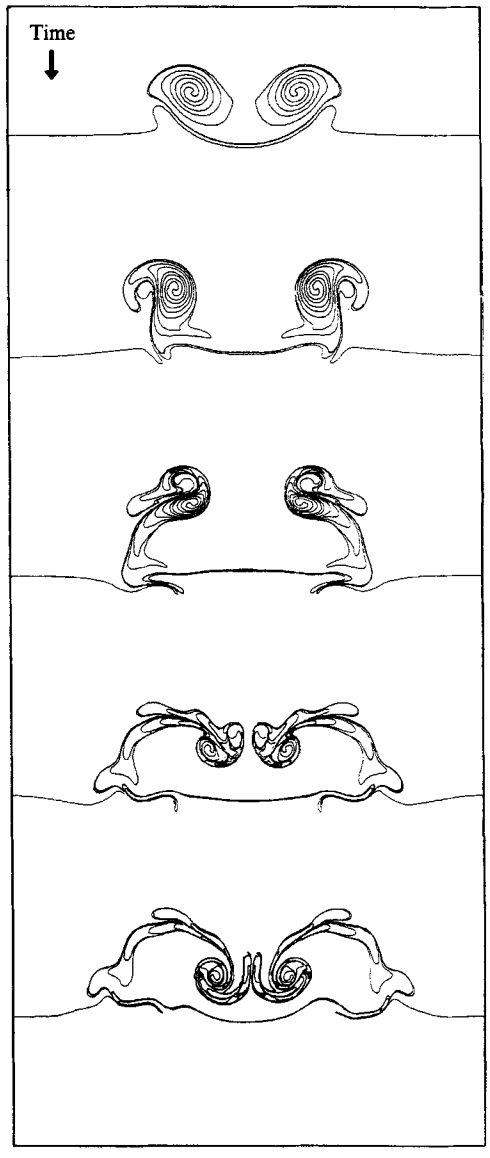

FIGURE 27. Computational sequence showing vortex pair interaction for $AR = 0.10$ in a wide computational box. Notice that, as the vortex pair reaches the interface, it pulls up part of the vortex sheet on the interface, which then rolls up to form a secondary vortex with the opposite circulation.

simultaneous side and bottom views of the interaction at a transparent wall are recorded. Essentially the same observations of vortex ring interaction with a solid wall have very recently been reported by Walker *et al.* (1987). Such observations have also been presented by Cerra & Smith (1983), and can be traced at least as far back as Magarvey & MacLatchey (1964*b*). Harvey & Perry (1971), Boldes & Ferreri (1973) and Barker & Crow (1977) also give some results for the interaction of a vortex with a solid wall.

Perhaps the most striking feature of the evolution in the sequence in figure 26 is how closely it resembles the interaction with the fluid interface for the relatively

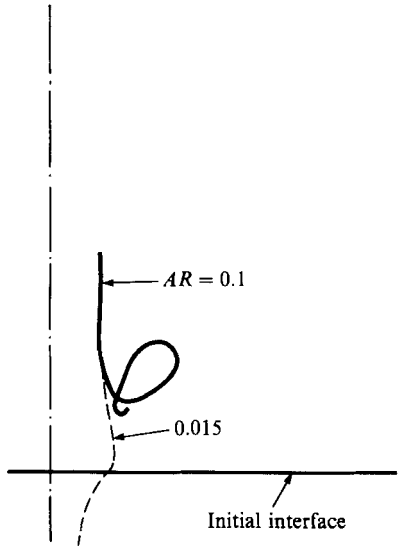

FIGURE 28. Computed trajectories of the primary vortices from the simulations in figures 21 and 27. Notice that for $AR = 0.015$ the vortex penetrates the interface and the cores are pushed together. For $AR = 0.1$, the vortex cores spread and rebound slightly. The trajectory for large AR can be compared with figure 11 of Walker *et al.* (1987) for the solid-wall case.

large value of AR in figures 8 and 12. In both cases, vorticity at the interface is swept up by the ring and forms a secondary vortex ring with the opposite sense of circulation. It is important to bear in mind that in figures 8 and 12 the vorticity is baroclinically generated at the interface, while in figure 26 it is generated as a result of the no-slip condition at the wall. The secondary ring in figure 26 orbits around and inside the original ring, and undergoes a similar Widnall-like instability as was noted in §4.2. The bottom view in the last photograph of this sequence clearly shows nine distinct azimuthal waves on the secondary ring after it has orbited to lie entirely inside the original ring. A third vortex ring can also be seen forming from interfacial vorticity, which follows a similar evolution as the secondary ring. Indeed, the entire interaction very nearly resembles that at a density interface for large values of AR. This is true despite the apparent difference in the mechanism by which secondary vorticity is generated.

In figure 26, we see a slight rebounding of the vortex from the wall, as was noted by Walker *et al.* (1987). This rebounding effect can also be seen in the interaction of a vortex at a density interface for large AR, as demonstrated in figure 27 where we show the long-time evolution in a wide computational box for the case $AR = 0.1$. The computed trajectory of the original vortex is shown in figure 28, which also gives the trajectory for $AR = 0.015$ from figure 21 for comparison. Note that, for the smaller value of AR, this figure clearly shows how the vortices are pushed together as they penetrate the interface. For the larger value of AR, the generation of secondary vortices from interfacial vorticity and their subsequent interaction with the original vortex causes the original vortex to rebound. Note that diffusion of vorticity from the interface is not essential for this process. Even if the fluid were inviscid, as is the case in these numerical simulations, if the original vortex can deform the interface, then the vortex sheet bound to the interface can be swept up to form secondary vortices and produce the subsequent rebounding of the original vortex when AR is large. This will remain true except for the interaction with a solid wall, in which case

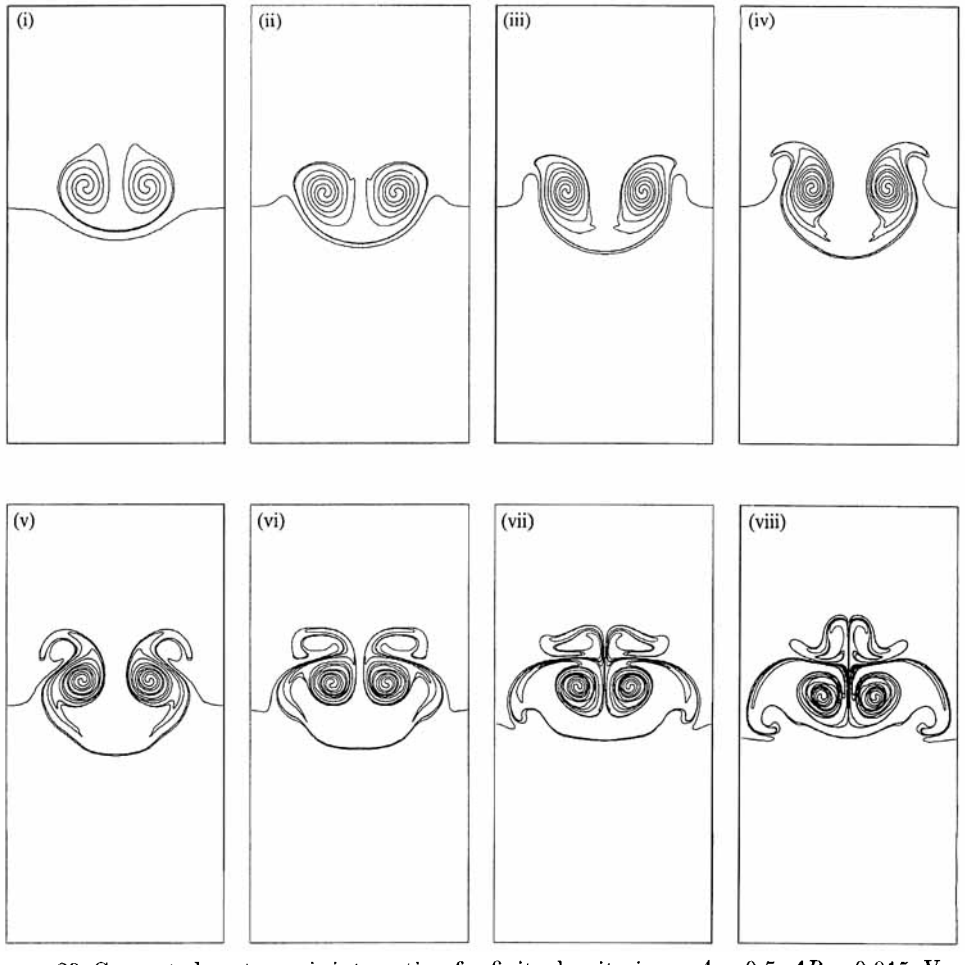

FIGURE 29. Computed vortex pair interaction for finite density jump $A = 0.5$, $AR = 0.015$. Vortex propagates downwards through the light (top) fluid into the heavy (bottom) fluid. Compare with figure 21, which shows the same AR but for the Boussinesq limit $A \to 0$, to see effects of the finite density jump. Notice that the penetration is reduced. Compare also with figure 30.

the vortex sheet is manifestly flat and cannot be deformed into secondary vortices unless viscosity is present to allow vorticity diffusion away from the wall. The resulting interaction at the wall is quite different from the classical potential flow result obtained by replacing the wall with an image vortex.

4.7. *Finite density jump*

Only in the limit of weak interface strength is the interaction determined by the one similarity parameter AR. Furthermore, it is only in this Boussinesq limit that the interaction is symmetric with respect to the initial location and direction of propagation of the vortices. For larger density jumps, the density parameter A in (5) enters as an independent similarity parameter.

To investigate the effect of A on the resulting interaction dynamics we repeated the case $AR = 0.015$, shown previously for $A \to 0$ in figure 21, with the same initial conditions but with $A = 0.5$, so that the bottom fluid is now three times more dense than the top fluid. The resulting dynamics are shown in figure 29. A comparison of

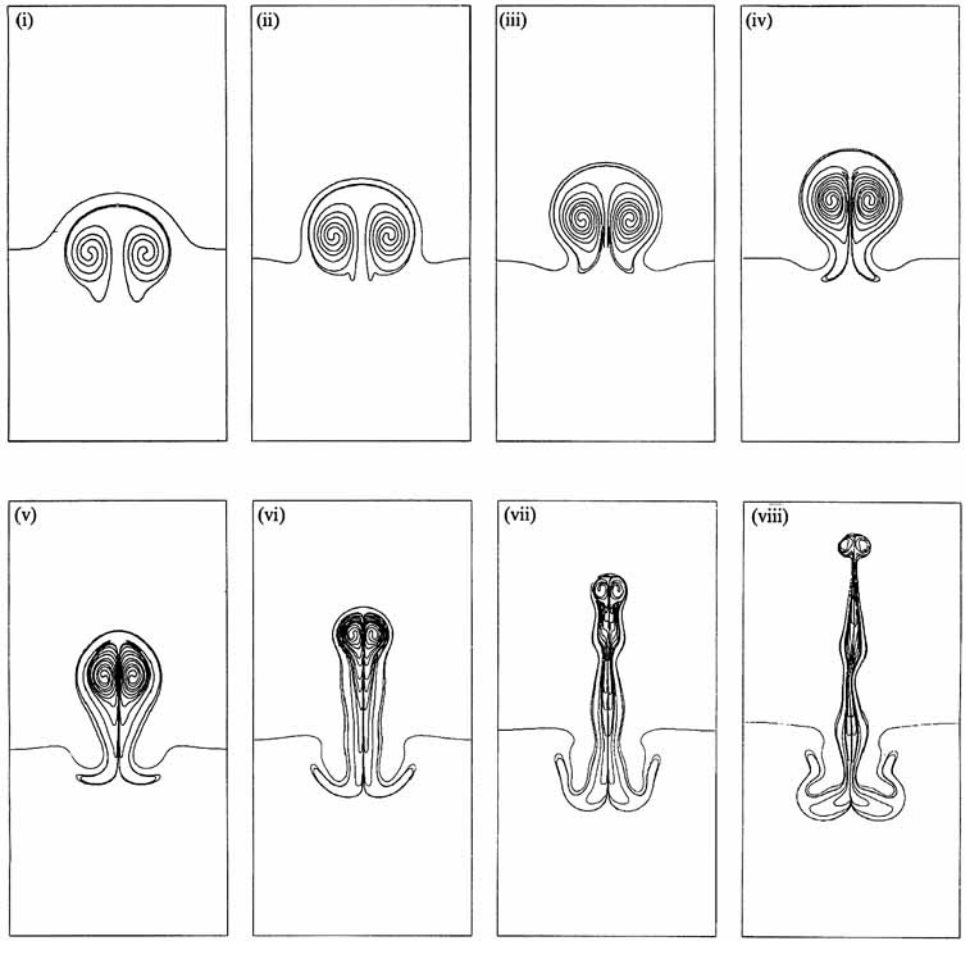

FIGURE 30. Computed vortex pair interaction for finite density jump $A = 0.5$, $AR = 0.015$. Similar to figure 29, but now the vortex propagates upward through the heavy (bottom) fluid into the light (top) fluid. Notice that the penetration is now enhanced in comparison with figure 21. Also, since the symmetry of the Boussinesq limit is no longer valid when the density jump is non-infinitesimal, note the loss of symmetry by comparing with figure 29.

these results shows that the relatively large density jump significantly affects the evolution. For $A = 0.5$ in figure 29, the vortex penetrates the interface considerably less and the backflow has a very different structure to that in figure 21.

To demonstrate the loss of inversion symmetry for such finite density jumps, figure 30 shows a similar case to figure 29, namely $AR = 0.015$ with the bottom fluid three times heavier than the top fluid, but now the vortex propagates upward from the heavy fluid into the light fluid. The loss of symmetry with respect to the light and heavy fluid locations is apparent in these results. The results suggest further that, when the vortex propagates from the heavier toward the lighter fluid, it penetrates through the interface considerably more than in figure 29. Note also that the Kelvin–Helmholtz instability of the backflow jet is now much less pronounced than in figure 21.

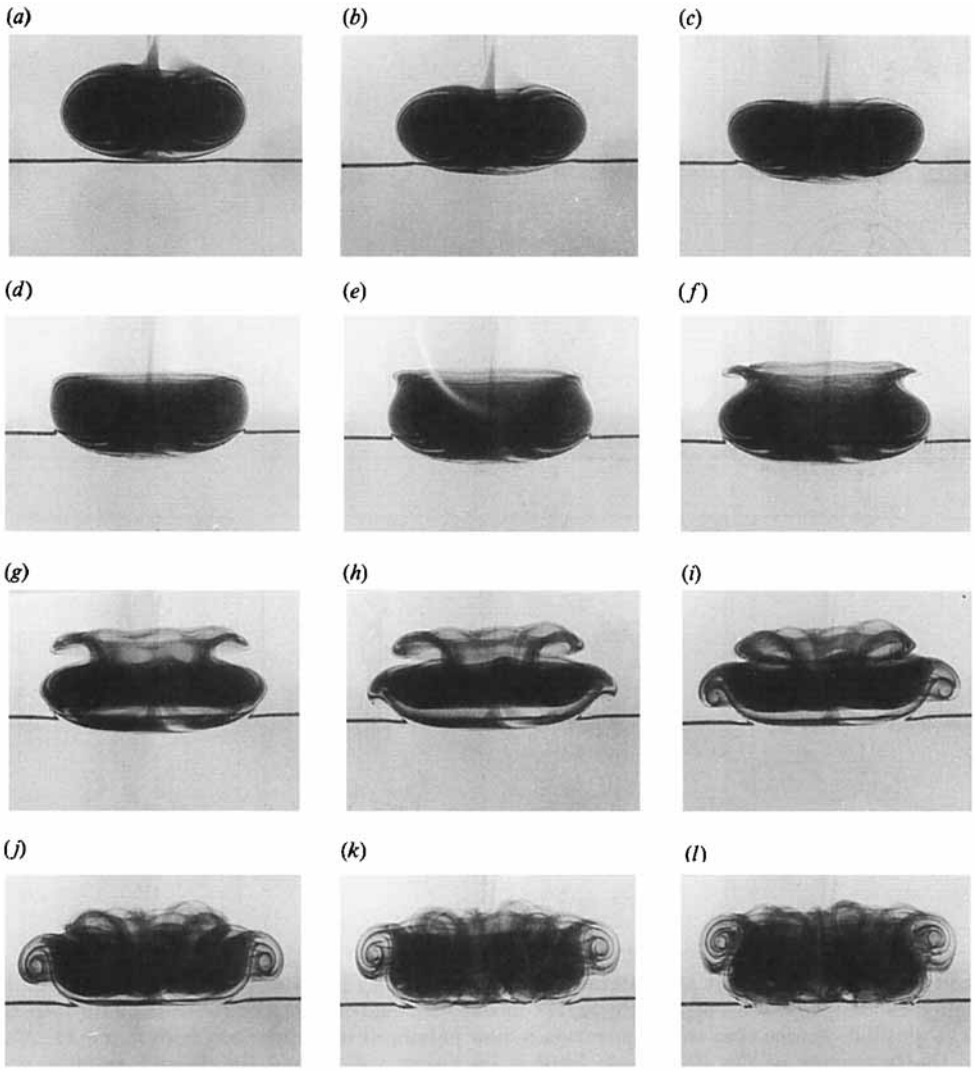

FIGURE 31. Photographic sequence showing the interaction of a vortex ring with a thick density interface $(\delta/a) = 0.5$ and $AR = 0.22$, giving $(a/\delta)AR = 0.44$. Compare with figure 32 to see the similarity in the stretched coordinate $y/(\delta/a)$. Note that the timescales differ by a factor of $\sqrt{2}$.

4.8. *Thick interfaces*

When the density interface is still sufficiently weak to be viewed in the Boussinesq limit $A \to 0$ but the interface thickness (δ/a) is no longer small then from (3), for any particular density gradient profile $f[y/(\delta/a)]$, the interaction should be governed by the similarity parameter $(a/\delta)AR$, and two cases with the same value of this similarity parameter should then be identical when viewed in the stretched coordinate $y/(\delta/a)$. The sequences in figures 31 and 32 show the interaction for two different cases in which the interface thickness δ is comparable to the ring diameter a. In figure 31, $(\delta/a) \approx 0.5$, $A = 0.0055$ and $R = 40.5$, while in figure 32 $(\delta/a) \approx 1.0$, $A = 0.0055$ and $R = 80.1$, so that in both cases $(a/\delta)AR = 0.44$. The solid line gives the initial position from which the interface diffused to its final thickness. The

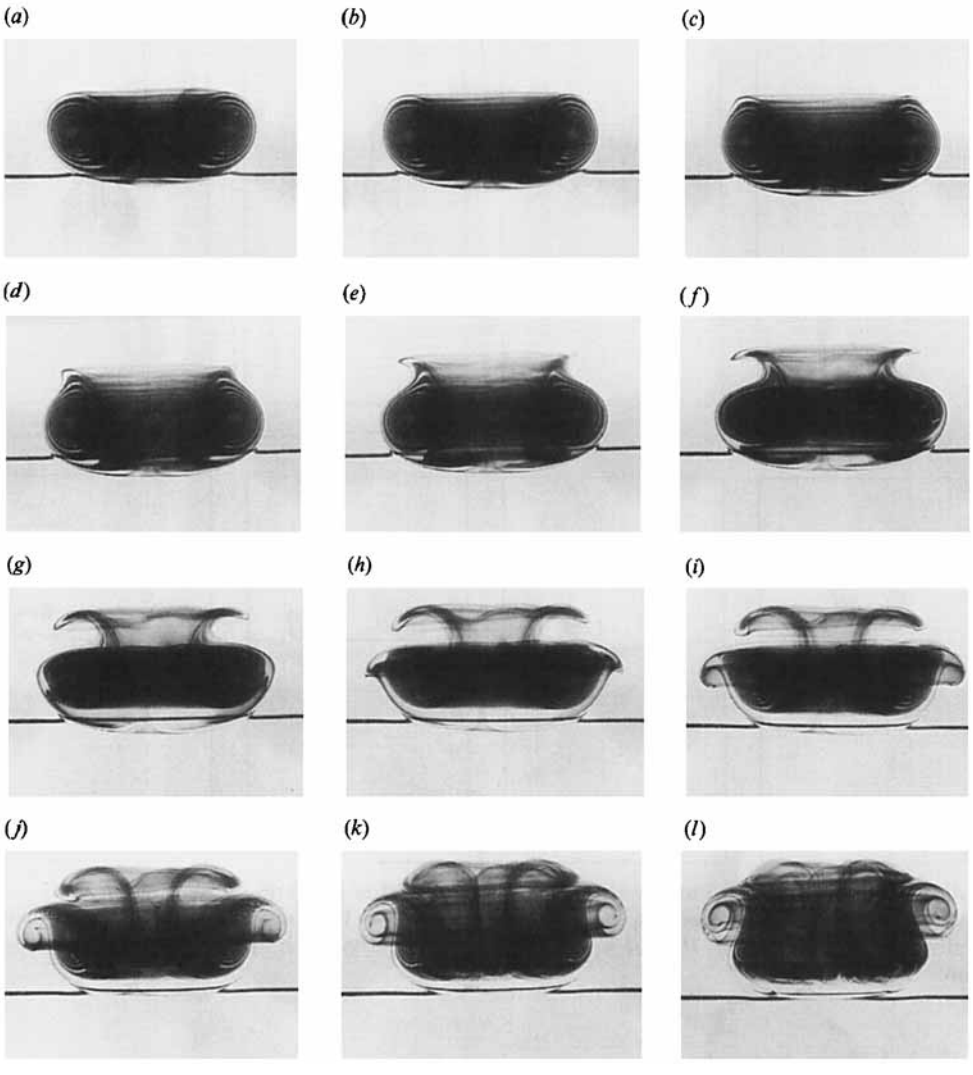

FIGURE 32. Photographic sequence showing the interaction of a vortex ring with a thick density interface. $(\delta/a) = 1.0$ and $AR = 0.44$, again giving $(a/\delta)\,AR = 0.44$. Compare with figure 31 to see the similarity in the stretched coordinate $y/(\delta/a)$.

density gradient profile $f[y/(\delta/a)]$ is essentially identical in these cases since both were obtained by simple diffusion from an initially thin interface. The interaction dynamics are indeed very nearly identical in these two cases in terms of the stretched coordinate $y/(\delta/a)$ and the dimensionless time. Note that since the circulations differ by the factor $\sqrt{2}$, the timescales also differ by this same factor. Also, as was noted in §4.2, the onset of the wavy instability in the secondary ring is Reynolds-number dependent and thus appears at a somewhat earlier dimensionless time in figure 31 than in figure 32. Note also that many features of the dynamics, including the formation and development of secondary and tertiary vortex rings from interfacial vorticity, are qualitatively similar to those observed for the thin interface limit in §4.2. The dynamics observed at a thick interface for a particular value of $(a/\delta)\,AR$ are, however, different from those seen for the same value of AR at a thin interface.

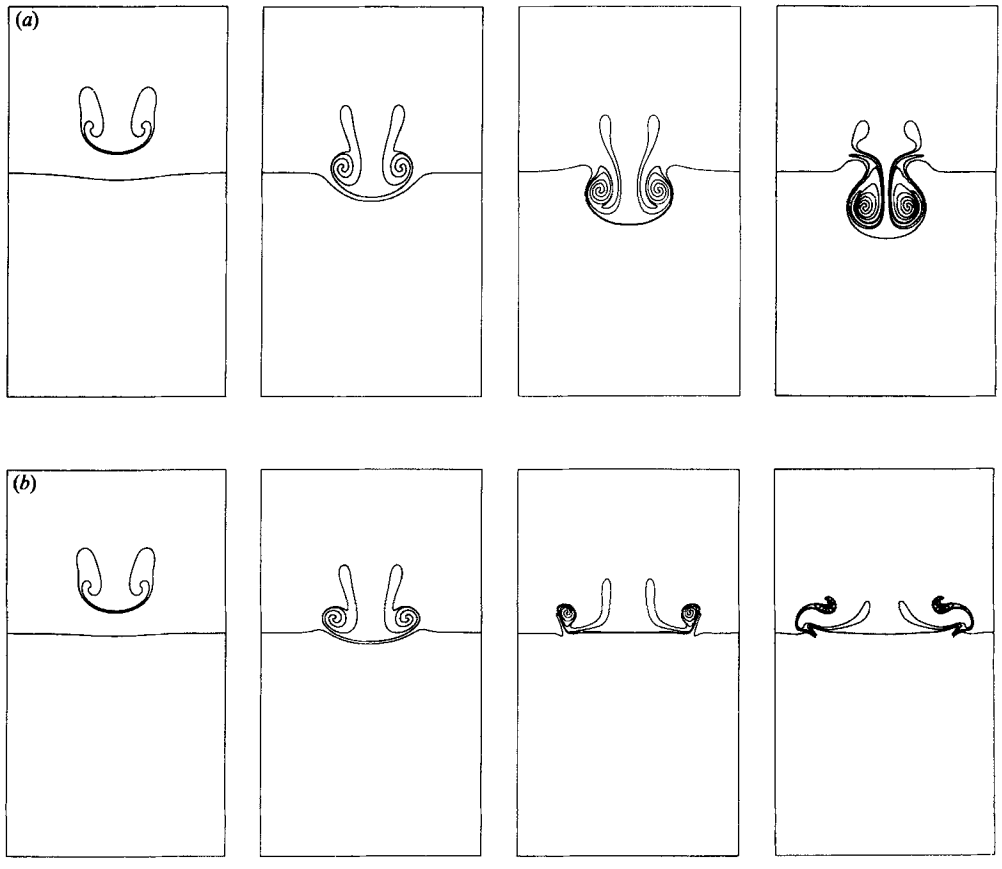

FIGURE 33. Axisymmetric numerical simulations of a vortex ring and its interaction with a thin density interface in the Boussinesq limit. (*a*) $AR = 0.04$; note the similarity with the experimental results in figures 5 and 9; (*b*) $AR = 0.4$; note the similarity with the experimental results in figures 8 and 12.

5. Concluding remarks

The experiments and numerical simulations in this study have identified the dynamical features of the interaction between a vortex and a density interface. The results have confirmed similarity arguments suggesting that, when the Reynolds number is large and surface tension is negligible, the interaction is governed by the two dimensionless parameters $(a/\delta)A$ and R. For thin interfaces $(\delta/a \to 0)$, the interaction becomes independent of the thickness and is determined by A and R. Furthermore, in the Boussinesq limit $A \to 0$, the interaction is governed solely by their product AR and is entirely invertible with respect to the initial location and direction of propagation of the vortices. Comparisons of our experimental and numerical results show a strong similarity between the interaction dynamics for planar vortex pairs and axisymmetric vortex rings, and suggest that many of the features observed here may apply to more general types of vortical flows.

However, our results also show some differences between the vortex ring experiments and the vortex pair calculations. It is natural to ask how many of these differences can be considered as being due to the different geometry and how many are due to phenomena not captured by the essentially inviscid numerical calculations,

such as vorticity diffusion and generation of vorticity by viscous stress gradients in the density interface. In figure 33 we show cross-sectional views of typical results from axisymmetric numerical simulations of vortex rings encountering a thin density interface in the Boussinesq limit, in this case for $AR = 0.04$ in figure 33(*a*) and $AR = 0.4$ in figure 33(*b*). The simulations were performed using an axisymmetric vortex blob method, with a rather large desingularization parameter. The initial condition was taken as a spherical vortex sheet with the strength again varying as the sine of the angle from the forward stagnation point. While this is probably not a very realistic representation of the initial condition in the experiments, which are not known precisely, it is the most natural extension of our two-dimensional simulations. Note that the fluid bounded by the vortex sheet rolls up into a ring, but here some of the initial fluid and vorticity is left behind as the ring forms. Part of this fluid is then drawn into the ring as it propagates downwards. This shedding of some of the fluid in the formation process is reminiscent of the formation observed in the experiments. The strengths of the rings in the cases shown here were selected so that the two limiting types of interactions described in §4.2 could be observed. In figure 33(*a*), the vortex ring is relatively strong in the sense that AR is rather small, while in figure 33(*b*) the ring is comparatively weak. The resulting dynamics are quite similar to those observed in the experiments and in the two-dimensional simulations. In figure 33(*a*) the ring penetrates the interface, its diameter decreases and some of the fluid is ejected back into the light fluid. In figure 33(*b*), however, the ring does not penetrate the interface but forms a secondary ring from interfacial vorticity. As this secondary ring and the original ring orbit around one another, note the reduction in cross-sectional area of the original ring as a consequence of continuity. This effect is, of course, not present in the two-dimensional cases. Axisymmetric simulations with a larger desingularization parameter show essentially the same behaviour. We can conclude from the agreement between our experimental and numerical results that many of the features of this class of interactions can be understood within the context of inviscid fluids, and that inviscid vortex methods can be used to accurately simulate many aspects of such interactions.

One of the most surprising findings in this study was the mechanism by which the lighter fluid is ejected back after being carried into the heavy fluid for small values of AR. Rather than the vortex simply rebounding and more or less retaining its shape, the outer layers are instead 'peeled' away, leaving increasingly less of the innermost part of the vortex intact. This peeling is driven by baroclinically generated vorticity at the sides of the crater formed by penetration of the vortex. The resulting vortex sheet which is ejected back into the lighter fluid is Kelvin–Helmholtz unstable and organizes into concentrated vortex structures which play a strong role in the subsequent evolution of the backflow. In the axisymmetric case, these vortex structures can undergo a Widnall-like instability driven by the destabilizing effect of compressional strain. Our results also show that as AR increases, the interaction dynamics tend towards a distinctly different limit. In this case, the vortex essentially does not penetrate through the interface, and the secondary and tertiary vortices which form tend to orbit around the original vortex. These results also demonstrate that the interaction dynamics at a density interface appear to become similar to the interaction at a solid wall in the limit as $A \to 0$ and $AR \to \infty$.

Lastly, we note that there are several obvious extensions to the work reported here. Examples include the whole family of oblique interactions, including the interactions that can result when the vortex initially moves parallel to the interface,

as well as the interaction for cases where $(\delta/a) \gg 1$ corresponding to a continuous stratification layer.

The experiments were supported with funds provided by The University of Michigan. The numerical simulations were supported by National Science Foundation Grant MSM-8707646, and were performed on the computers of the San Diego Supercomputing Center, which is sponsored by the NSF. We thank Mr Zhian Kuang for help with the axisymmetric calculations.

REFERENCES

BARKER, S. J. & CROW, S. C. 1977 The motion of two-dimensional vortex pairs in a ground effect. *J. Fluid Mech.* **82**, 659–671.

BATCHELOR, G. K. 1967 *Fluid Dynamics*. Cambridge University Press.

BOLDES, U. & FERRERI, J. C. 1973 Behavior of vortex rings in the vicinity of a wall. *Phys. Fluids* **16**, 2005–2006.

CERRA, A. W. & SMITH, C. R. 1983 Experimental observations of vortex ring interaction with the fluid adjacent to a surface. *Report FM-4*, Dept of Mech. Engng & Mech. Lehigh University.

CROW, S. C. 1970 Stability theory for a pair of trailing vortices. *AIAA J.* **8**, 2172–2179.

DAHM, W. J. A. & SCHEIL, C. M. 1987 Dynamics of vortex ring interaction with a density interface. *Bull. Am. Phys. Soc.* **32**, 2038 (abstract only).

DEEM, G. S. & ZABUSKY, N. J. 1978 Stationary V-states: Interactions, recurrence and breaking. *Phys. Rev. Lett.* **40**, 859.

FRAENKEL, L. E. 1970 On steady vortex rings of small cross section in an ideal fluid. *Proc. R. Soc. Lond.* A **316**, 29–62.

HARVEY, J. K. & PERRY, F. J. 1971 Flowfield produced by trailing vortices in the vicinity of the ground. *AIAA J.* **9**, 1659–1660.

HECHT, A. M., BILANIN, A. J., HIRSH, J. E. & SNEDEKER, R. S. 1980 Turbulent vortices in stratified fluids. *AIAA J.* **18**, 738–746.

HECHT, A. M., BILANIN, A. J. & HIRSCH, J. E. 1981 Turbulent trailing vortices in stratified fluids. *AIAA J.* **19**, 691–698.

HILL, F. M. 1975 A numerical study of the descent of a vortex pair in a stably stratified atmosphere. *J. Fluid Mech.* **71**, 1–13.

KRASNY, R. 1986 Desingularization of periodic vortex sheet roll-up. *J. Comp. Phys.* **65**, 292–313.

KRAUCH, T. 1980 Die Bildung eines Ringwirbels an einer kreisförmigen Düsenmündung and seine Umbildung beim Aufstieg in einer Flüssigkeitsschicht und an der Flüssigkeitsoberfläche. *Strömungsforschung Max-Planck Institut*, Göttingen.

KRUTZSCH, C.-H. 1936 Über ein instabiles Gebiet bei Wirbelringen. *Z. angew. Math. Mech.* **16**, 352–353.

KRUTZSCH, C.-H. 1939 Über eine experimentell beobachtete Erscheinung an Wirbelringen bei ihrer translatorischen Bewegung in wirklichen Flüssigkeiten. *Ann. Phys.* **35**, 497–523.

LAMB, H. 1945 *Hydrodynamics*. Dover.

LEONARD, A. 1980 Vortex methods for flow simulation. *J. Comp. Phys.* **37**, 289–335.

LEONARD, A. 1985 Computing three-dimensional incompressible flows with vortex elements. *Ann. Rev. Fluid Mech.* **17**, 523–559.

LINDEN, P. F. 1973 The interaction of a vortex ring with a sharp density interface: a model for turbulent entrainment. *J. Fluid Mech.* **60**, 467–480.

MACGARVEY, R. H. & MACLATCHY, C. S. 1964*a* The formation and structure of vortex rings. *Can. J. Phys.* **42**, 678–683.

MACGARVEY, R. H. & MACLATCHY, C. S. 1964*b* The disintegration of vortex rings. *Can. J. Phys.* **42**, 684–689.

MAXWORTHY, T. 1972 The structure and stability of vortex rings. *J. Fluid Mech.* **51**, 15–32.

MAXWORTHY, T. 1977 Some experimental studies of vortex rings. *J. Fluid Mech.* **81**, 465–495.

MOORE, D. W. & SAFFMAN, P. G. 1975 The instability of a straight vortex filament in a strain field. *Proc. R. Soc. Lond.* A **346**, 413–425.

SAFFMAN, P. G. 1970 The velocity of viscous vortex rings. *Stud. Appl. Maths* **49**, 371–380.

SAFFMAN, P. G. 1972 The motion of a vortex pair in stratified atmosphere. *Stud. Appl. Maths* **2**, 107–119.

SAFFMAN, P. G. 1978 The number of waves on unstable vortex rings. *J. Fluid Mech.* **84**, 625–639.

SAFFMAN, P. G. 1979 The approach of a vortex pair to a plane surface in inviscid fluid. *J. Fluid Mech.* **92**, 497–503.

SAFFMAN, P. G. & BAKER, G. R. 1979 Vortex interactions. *Ann. Rev. Fluid Mech.* **11**, 95–127.

SARPKAYA, T. 1983 Trailing vortices in homogeneous and density-stratified media. *J. Fluid Mech.* **136**, 85–109.

SULLIVAN, J. P., WIDNALL, S. E. & EZEKIEL, S. 1973 Study of vortex rings using a laser doppler velocimeter. *AIAA J.* **11**, 1384–1389.

TOMOKITA, S. 1936 Instability and breaking up of a ring of an incompressible perfect fluid. *Proc. Phys. Math. Soc. Japan* **18**, 535–549.

TRYGGVASON, G. 1987 Interaction of vorticity and density interfaces. *Bull. Am. Phys. Soc.* **32**, 2073 (abstract only).

TRYGGVASON, G. 1988*a* Deformation of a free surface as a result of vortical flows. *Phys. Fluids* **31**, 955–957.

TRYGGVASON, G. 1988*b* Numerical simulations of the Rayleigh-Taylor instability. *J. Comput. Phys.* **75**, 253–282.

TRYGGVASON, G. 1989 Simulations of vortex sheet rollup by vortex methods. *J. Comput. Phys.* **80**, 1–16.

WALKER, J. D. A., SMITH, C. R., CERRA, A. W. & DOLIGALSKI, T. L. 1987 The impact of a vortex ring on a wall. *J. Fluid Mech.* **181**, 99–140.

WIDNALL, S. E. & SULLIVAN, J. P. 1973 On the stability of vortex rings. *Proc. R. Soc. Lond.* A **332**, 335–353.

WIDNALL, S. E., BLISS, D. B. & TSAI, C.-Y. 1974 The instability of short waves on a vortex ring. *J. Fluid Mech.* **66**, 35–47.

YIH, C.-S. 1975 Vortices and vortex rings of stratified fluids. *SIAM J. Appl. Maths* **28**, 899–912.